ENGINEERING OF RUDDLESDEN-POPPER PLANAR FAULTS IN $CsPbBr_3$ PEROVSKITE NANOCRYSTALS FOR IMPROVED PERFORMANCE IN LIGHT EMITTING DEVICES

A Dissertation

presented to

the Faculty of the Graduate School

at the University of Missouri – Columbia

In Partial Fulfillment

of the Requirements for the Degree

Doctor of Philosophy

---

by

MARIIA GORIACHEVA

Dr. Yangchuan Xing, Dissertation Supervisor

MAY 2021

The undersigned, appointed by the dean of the Graduate School, have examined the dissertation entitled

ENGINEERING OF RUDDLESDEN-POPPER PLANAR FAULTS IN $CsPbBr_3$ PEROVSKITE NANOCRYSTALS FOR IMPROVED PERFORMANCE IN LIGHT EMITTING DEVICES

presented by Mariia Goriacheva,

a candidate for the degree of doctor of philosophy,

and hereby certify that, in their opinion, it is worthy of acceptance.

Professor Yangchuan Xing

Professor Patrick Pinhero

Professor Sheila Grant

Professor Heather Hunt

Professor Suchismita Guha

ACKNOWLEDGEMENTS

I would like to express my deep appreciation to my advisor Dr. Yangchuan Xing for his valuable mentorship, continuous guidance and tremendous support. I treasure the experience and knowledge I gained from you. You have given me so many opportunities, and for that, I will always be grateful to you.

I would like to express my sincere gratitude to Dr. Suchismita Guha for welcoming me into her group and providing so much needed platform for experimental work. I thank you for the utmost contribution to the advancement of my research and the indispensable discussions. I have gained a lifelong mentor in you.

I thank Dr. Patrick Pinhero, Dr. Sheila Grant, Dr. Heather Hunt and Dr. Suchismita Guha for their willingness to be members of my thesis committee. I am grateful for your much appreciated time and valuable advice allowing me to complete this work.

I would like to extend my thanks to Dr. Alexander Safronov and Dr. Peter Cornish, who kindly provided me with a free access to their equipment. I would also like to thank Dr. Tommi White and Dr. Xiaoqing He for a prosperous collaboration.

I wish to thank all current and former students in Dr. Xing’s and Dr Guha’s groups for their support and contribution to my achievements.

I wish to express my appreciation to the staff of Chemical Engineering Department for providing a great learning environment. I would like to thank all who contributed to my educational and personal growth at the University of Missouri.

Lastly, I would like to thank my husband, Joshua Morrell, for his unconditional love and endless support.

TABLE OF CONTENTS

LIST OF ILLUSTRATIONS

LIST OF TABLES

ENGINEERING OF RUDDLESDEN-POPPER PLANAR FAULTS IN $CsPbBr_3$ PEROVSKITE NANOCRYSTALS FOR IMPROVED PERFORMANCE IN LIGHT EMITTING DEVICES

Mariia Goriacheva

Dr. Yangchuan Xing, Dissertation Supervisor

ABSTRACT

We developed a procedure that allowed triggering post-synthetic growth of $CsPbBr_3$ perovskite nanocrystals (PNCs) via fusion. Pursuing the study, we discovered that the growth of $CsPbBr_3$ PNCs was accompanied by the formation of Ruddlesden-Popper (RP) planar faults – well known for perovskite oxides, yet not observed in perovskite all-inorganic halides until then. In a mutual effort with the researchers at the University of Washington, it was discovered that the RP planar faults were predicted to produce significant band-off sets in the conduction (+134 meV) and valence bands (-193 meV), thus repelling both electrons and holes at room temperature. In other words, RP faults were projected to serve as built-in potential wells, confining excitons within the perovskite domains. Following this lead, we proceeded exploration of $CsPbBr_3$ PNCs with RP planar faults with an intent to define the impact of such RPs on the optoelectronic properties of $CsPbBr_3$ PNCs.

The work consists of three parts. In part one, we analyze and provide further support to the suggested earlier mechanism behind the formation of the RP faults. We demonstrate that the injection of diethylzinc into the PNCs solution results in a removal of stabilizing ligands from the surface of the PNCs, and their subsequent fusion accompanied with the formation of RPs. By modifying the procedure, we find that the concentration of the occurring RPs is higher when the injection is performed in the excess of CsBr. We reveal that the in the

absence of high moisture content RP-$CsPbBr_3$ PNCs display an extraordinary resilience to photodegradation when compared to PNCs without RPs. In addition, we demonstrate that the RP-$CsPbBr_3$ PNCs can undergo anion-exchange reaction while successfully preserving the RP faults. This discovery opens up the avenue for future exploration of the observation for the first time mixed $CsPb(I/Br)_3$ PNCs with RP planar faults.

In part two, we study optoelectronic properties of RP-$CsPbBr_3$ PNCs with an attempt to define the structure-property relationship for PNCs with the RPs. Our findings reveal that RP-$CsPbBr_3$ PNCs exhibit higher binding energies and longer exciton lifetimes. The former is attributed to the quantum confinement induced by the RPs, resulting in tightly bound excitons within the perovskite domains cleaved by the RPs. The latter is ascribed to a plausible electron-hole spatial separation across the RP fault analogous to the one reported for quantum dots with the type II energy alignment. We also study the up-conversion photoluminescence in both types of PNCs and reveal a significant difference in the response. These findings demonstrate explicitly that the RP faults largely transform optoelectronic properties of $CsPbBr_3$ PNCs. Higher binding energies and longer lifetimes, combined with the exceptional resilience to photodegradation establish the RP-$CsPbBr_3$ PNCs as excellent candidates for light emitting devices (LEDs).

In part three, we postulate and experimentally verify the enhanced performance of RP-$CsPbBr_3$ PNCs in thin-film perovskite LEDs. Both type of PNCs are put to a test in the devices with identical architectures. We demonstrate that RP-LEDs outperform LEDs without RP faults. Specifically, they display stronger electroluminescence response, significantly higher air stability and better reproducibility. This is the first demonstration of thin-film LEDs based on all-inorganic $CsPbBr_3$ PNCs with RP planar faults.

Lastly, we summarize our findings and conclude the work with the suggestions for future work.

CHAPTER I. LITERATURE REVIEW

1.1 Introduction

First exploration of tri-halide perovskite materials with the formula $CsPbX_3$ (X = Cl, Br or I) goes back to 1893 featuring pioneering work of Wells [1]. While the material was known for more than a century, it did not gain wide attention until recent discovery of its colloidal form by the group of M. Kovalenko [2]. Since then an unprecedented research was launched providing a platform for new discoveries. Inorganic tri-halide perovskite nanocrystals (PNCs) revealed abundant optoelectronic properties, including but not limited to strong optical absorption, remarkably bright photoluminescence, high quantum yield, tunable band gap, and defect tolerant physics [3]. $CsPbX_3$ PNCs showed promise in a variety of optoelectronic devices, including solar cells, light-emitting diodes (LED), photodetectors, and lasers [3-6].

One of the key limiting factors for the performance of the optoelectronic device is the presence of defects in the semiconductor. However, certain defects can be successfully employed toward enhancement of the device performance. Doping of conventional semiconductors is an excellent example of such improvement. Thus understanding the nature and the role of defects in crystal structure is imperative for the development of optoelectronic applications.

Extensive research on atomistic structure of $CsPbBr_3$ PNCs revealed that most of the intrinsic point defects induce shallow transition states, whereas deep level defects are rare due to their high formation energy [7]. Planar defects, such as Ruddlesden-Popper (RP) planar faults, have been observed in perovskite oxides and were linked to some unique properties (examples are provided in Chapter 1.2). Plausible existence of an RP phase in $CsPbBr_3$ PNCs was initially predicted by Yu *et al.* in 2017 [8]. Later, a few groups, including ourselves, experimentally developed such RPs in all-inorganic PNCs [9-11]. Furthermore, in joint effort with our collaborators we demonstrated that RP faults significantly altered optoelectronic properties of $CsPbBr_3$ PNCs [9, 12]. Herein, we summarize the existing knowledge on the Ruddlesden-Popper phase in all-inorganic perovskites in the attempt to define structure-property relationship between the RP phase and the optoelectronic properties of $CsPbBr_3$ PNCs.

1.2 Ruddlesden-Popper Phase in Perovskite Oxides

The structure of Ruddlesden-Popper phase was first synthesized and described by S.N. Ruddlesden and P. Popper in 1957 [13]. In general, the RP phase represents a layered structure and results from the intergrowth of a perovskite-type and a rocksalt-type structure. Perovskite structure with general formula ABX_3 consists of cation B surrounded by an octahedron out of anions X sited in a cube out of cations A; rocksalt-type structure with a general formula AX is made out of cation A and anion X. When an RP phase is formed, a perovskite layer is interleaved with rock-salt type layers, where AX layers are shifted by ½ a unit cell respectively [14] (Fig. 1.1). Such unit shift results in a formation of a planar defect named Ruddlesden-Popper (RP) fault. RP faults were commonly observed in perovskite oxide compounds, and were thought to originate in several interesting properties.

As such, for a long time high temperature superconductivity was associated with the essential presence of copper in the perovskite structure until the discovery of non-copper perovskite compounds exhibiting superconductivity at temperatures as high as 30K [15].

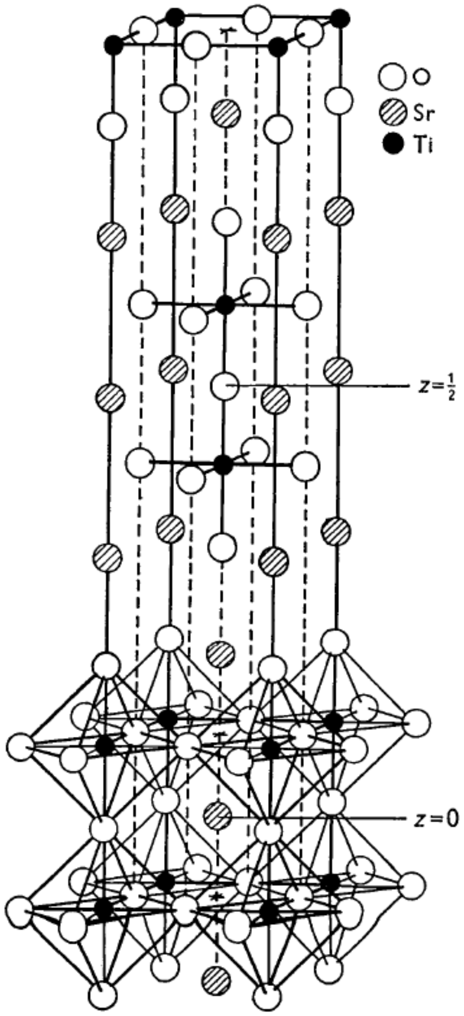

Figure 1.1 Crystallographic structure of the RP phase based on $Sr_3Ti_2O_7$ compound, where the perovskite layers are shifted by ½ a unit cell with respect to each other [14].

Interestingly, all known superconductors, regardless of copper presence, were found to possess an RP phase. Therefore, it has been hypothesized that the superconductivity could arise from the defect nature of the crystal [16].

Later, the RP-type perovskite crystals were found to exhibit colossal magnetoresistance (CMR) effect that could not be explained by generally accepted theory of complete ferromagnetic order or zero-field metal-insulator transitions, thus demanding further scrutiny of the origin of the CMR effect in perovskites [17].

Most recent exploration of RP-type perovskite oxides revealed their potential to serve as a reversible air electrode catalyst in rechargeable metal-air batteries [18]. Due to an easy removal of oxygen present in RP-$LaSr_3Fe_3O_{10}$, reversible oxygen reactions (reduction and evolution) were achieved with minimal efficiency losses. Hence, RP-type perovskite oxides are expected to enhance the efficiency of rechargeable Al-air batteries in the future.

Though full understanding of crystal structure-property relationship has not been achieved yet, it is believed that the newly found properties are associated with the RP phase in the crystal structure. Thus, the exploration of an RP phase in perovskite halides is significant as it can reveal unrealized potential of all-inorganic perovskite halides.

1.3 Ruddlesden-Popper Phase in All-inorganic Perovskite Halides

The plausible existence of the RP phase in $CsPbBr_3$ PNCs was first predicted by the group of researchers at Berkeley, California [8]. Using state-of-the-art aberration-corrected scanning transmission electron microscopy (AC-STEM) they directly observed coexistence of conventional perovskite phase and a plausible RP phase in 2D $CsPbBr_3$ nanosheets. Though the technology did not allow to estimate the thickness of perovskite layers, a reliable model of conceivable RP phase in $CsPbBr_3$ was proposed (Fig. 1.2).

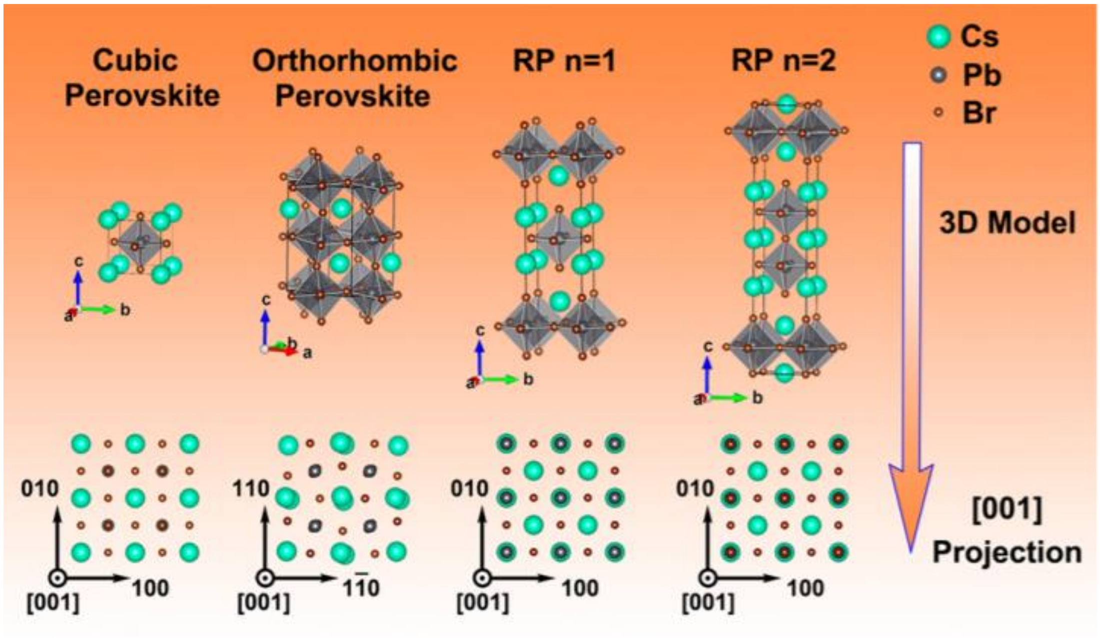

Figure 1.2. 3D Illustration of crystal structures of conventional perovskite (cubic and orthorhombic) and the RP (n=1, 2) phases with their corresponding [001] projections. The perovskite $CsPbBr_3$ phase is depicted by pure Cs and Pb-Br columns, the RP CsBr phase is composed of Cs-Pb (n=1) and Cs-Pb-Br (n=2) columns [8].

The authors revealed that in a conventional perovskite phase in [001] projection, the structure was depicted by pure Cs and Pb-Br columns, whereas in the RP phase the columns were composed of Cs-Pb for n=1 and Cs-Pb-Br for n=2, where n equals the number of perovskite layers interleaved with the RP phase. This allowed visual differentiating of the

RP phase from a conventional perovskite phase, both coexisting in a crystal. Further STEM image-based simulations demonstrated a close match between experimental and theoretical models (Fig. 1.3). Such phases were separated by domain boundaries, i.e. RP planar faults, observed as straight or step-like lines, and comprised of Cs and Br ions.

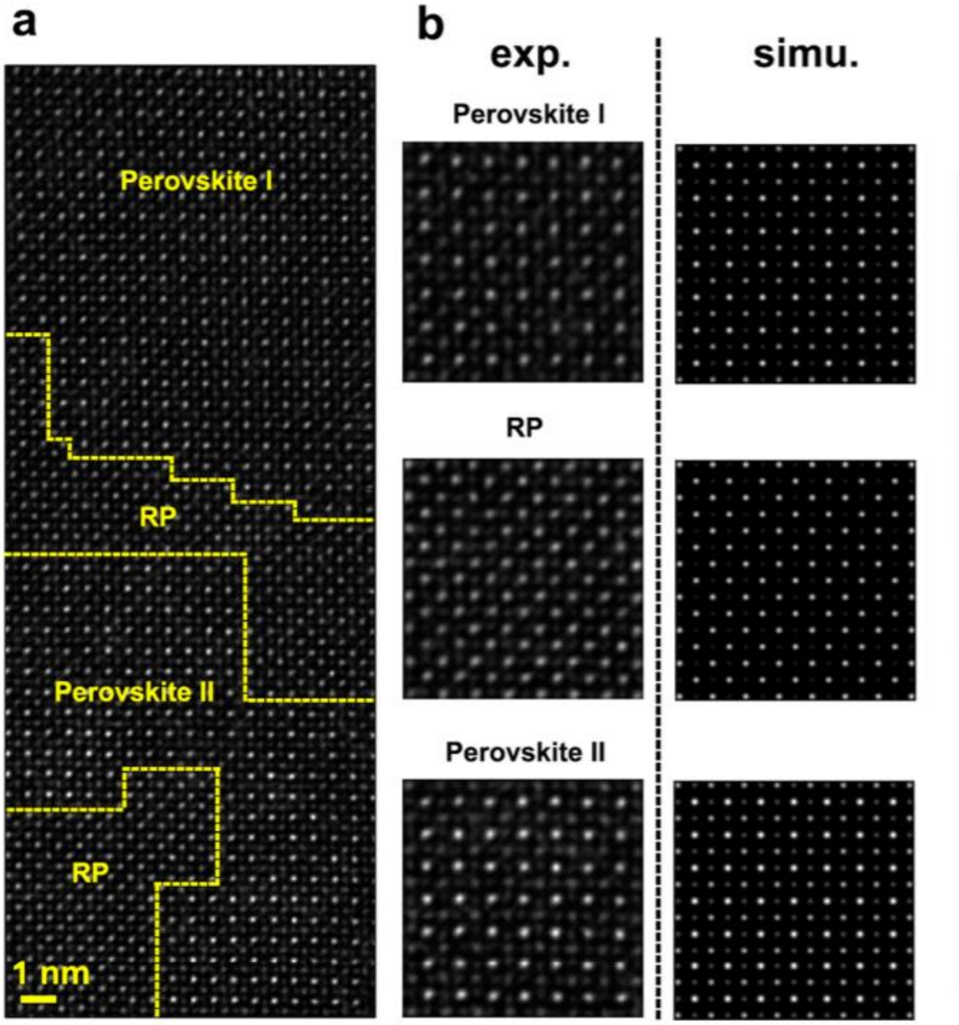

Figure 1.3. (a) Typical STEM image of 2D $CsPbBr_3$ nanosheet depicting coexistence of the perovskite and RP phases. Domain boundaries are indicated by yellow dotted lines. (b) Comparison between experimental and simulated images. Images correspond to close up domains depicted in panel a. From top to bottom: six-layer perovskite phase, one-layer n=2 RP phase, and six-layer $–PbBr_3$-teminated perovskite phase [8].

At the time the plausible model was presented, there was no known experimental route to develop such RP phases in $CsPbBr_3$ nanocrystals. Later Manna *et al.* demonstrated that the formation of RP phases in all-inorganic perovskite halides could be achieved via mixing I ions with Cl, or with Br and Cl ions prior to PNCs formation [10]. Such method produced alloyed $Cs_2PbI_2Cl_2$ and $CsPb(Cl:Br:I)_3$ PNCs with RP faults. $Cs_2PbI_2Cl_2$ PNCs displayed an extremely strong excitonic absorption despite a relatively large size (5 nm thick with 40 nm in lateral dimensions), which was attributed to the confinement of Pb-Cl perovskite layers by the RP phase (Fig. 1.4).

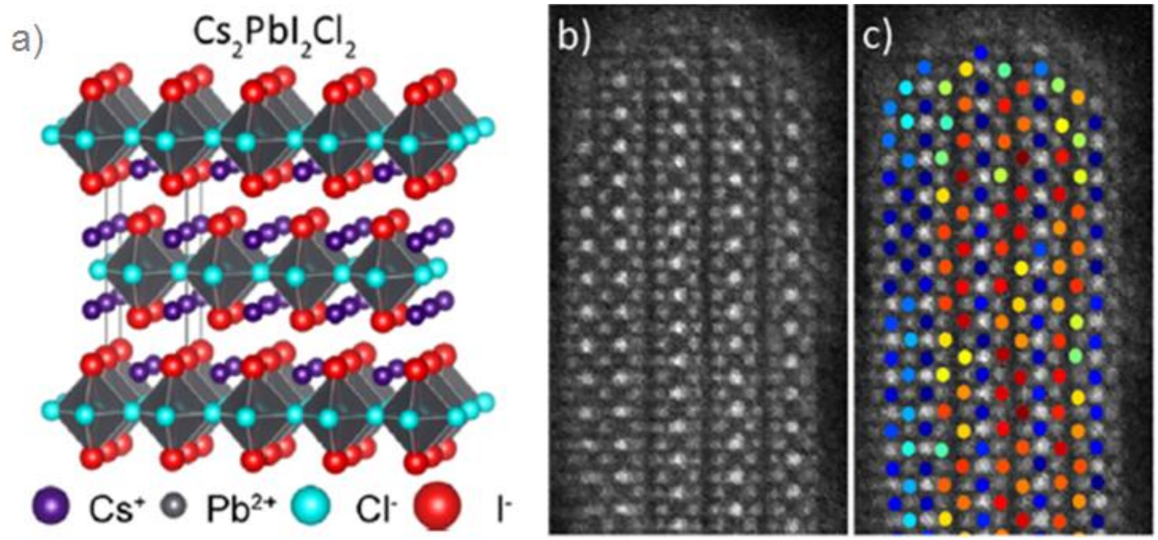

Figure 1.4. (a) 3D illustration of mixed $Cs_2PbI_2Cl_2$ PNC showing formation of RP phases. (b) HAADF-STEM image displaying side view of the PNC with its corresponding atomic arrangement shown in panel (c) [10].

Triple halide CsPb(Cl:Br:I)$_3$ PNCs displayed a very low quantum yield (QY) of 0.1%. Poor photoluminescence (PL) response was ascribed to the origin of the PR planar faults. Triple halides predominantly crystalized in a conventional perovskite structure, similar to CsPbBr$_2$Cl, while only small amount of I ions was incorporated into its structure. Due to significant size difference, I ions migrated from the perovskite structure to the inner surface where they formed an RP planar fault (Fig. 1.5). The segregation of I ions to the interface of the perovskite phase resulted in significant changes in the structure of the band gap of the PNCs, pushing I atomic orbitals below the valence band edge.

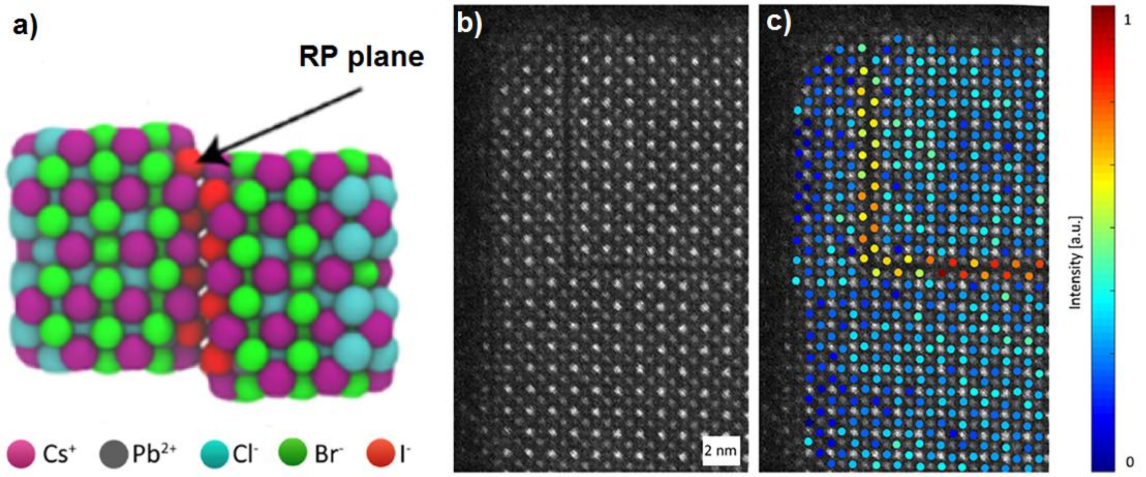

Figure 1.5. (a) 3D illustration of mixed CsPb(Cl:Br:I)$_3$ PNC showing formation of the RP phase. (b) HAADF-STEM image displaying side view of the PNC with its corresponding atomic arrangement show in panel (c). Brighter atoms correspond to I ions migrating outside the perovskite phase [10].

Authors postulated that the significant loss in QY was most likely due to the presence of halide vacancies in the RP plane, which could result in the formation of deep level trap states capable of trapping excitons. Such problem is usually resolved by additional passivation of trap sites with organic surfactants. However, given the location of RP faults deep inside the $CsPb(Cl:Br:I)_3$ crystal such approach is not feasible in this case.

Most recent work by Feldmann *et al*. demonstrated that doping $CsPbCl_3$ PNCs with Mn^{2+} was also accompanied by the formation of RP planar faults [11]. Interestingly, the number of RP faults was directly proportional to the concentration of the dopant added – the higher the concentration of Mn^{2+} , the more RPs were observed. Authors postulated that RP faults resulted from the size difference between Mn^{2+} (1.6 Å) and Pb^{2+} (2.38 Å) cations, and the limited availability of Pb^{2+} in the abundance of Mn^{2+}. As a result, RP planes comprised out of Cs^+ and Cl^- ions were produced. Preceding the works of Manna and Feldman, we demonstrated that the RP faults in $CsPbBr_3$ PNCs could be successfully formed via inducing post-synthetic growth of the latter [9]. A detailed study on the procedure and the outcomes are presented in Chapter 2.

When our samples were studied by collaborators at the University of Washington, they observed RP faults and their plausible role in charge transport in the RP-$CsPbBr_3$ PNCs [12]. Using high-angle annular dark field (HAADF) STEM, Thind *et al.* confirmed the presence of RP planar defects and showed that the RP planar fault could propagate along the (010) and (100) planes throughout the $CsPbBr_3$ PNCs and form a 90° step (Fig. 1.6a, b). Z-contrast atomic assignment in Figure 1.6c clearly shows the rocksalt-type structure of the RP phase comprised out of two CsBr layers, shifted by half a unit cell with respect to each other, and bordered with $CsPbBr_3$ perovskite domains on either side. In addition, the authors developed DFT-optimized atomic structure of the RP planar fault (shown in

Figure 1.6d), and found the average layer distance between the CsBr layers to be 3.70Å, which was in a good agreement with the experimental value of 3.59 Å.

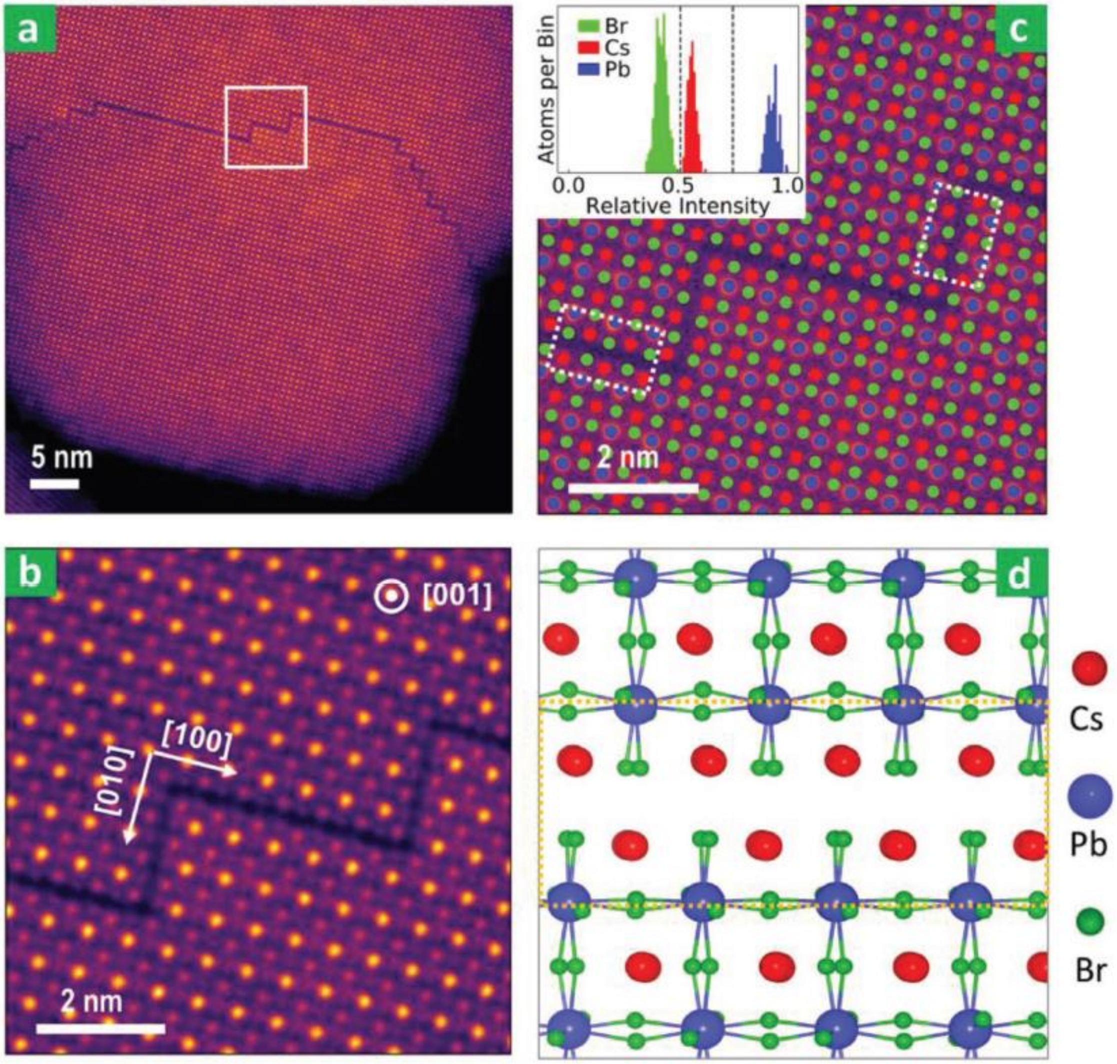

Figure 1.6. (a) Low-resolution HAADF image of the RP planar fault propagating across the RP-$CsPbBr_3$ PNC. (b) Atomic-resolution HAADF image of a selected region indicated by the white square in panel a. (c) Atomic assignment of the structure in panel b according to the Z-contrast intensities. (d) DFT-optimized model of the RP planar fault [12].

The HAADF STEM images were obtained by elastic scattering of the electron beam from different atomic columns (Cs, Pb, and Br), where the degree of elastic scattering is approximately proportional to the squared atomic number ($\sim Z^2$) [19]. Hence, Pb (Z=82) atomic columns appeared the brightest in the images, followed by Cs (Z=55) and Br (Z=35). Using obtained images in combination with the first-principles DFT calculations, the authors revealed significant changes in electronic properties of $CsPbBr_3$ PNCs originating from the RP planar faults. Their findings are summarized in the next chapter.

1.4 Electronic Properties of $CsPbBr_3$ Perovskite Nanocrystals with Ruddlesden-Popper Planar Faults

Since planar defects in traditional semiconductors can serve as a sink for point defects [20-22], often impeding charge transport and facilitating non-radiative recombination, understanding the nature of the newly discovered RP planar fault in $CsPbBr_3$ is paramount for optoelectronic applications.

Based on our RP-$CsPbBr_3$ PNCs Thind *et al.* demonstrated that the experimentally developed RP faults did not introduce any deep level defects in the bandgap [12]. They also studied several additional structures by introducing Cs and/or Br vacancies to the experimentally produced RP planar faults as shown in Figure 1.7. Interestingly, neither pure Cs vacancies nor combination of Cs and Br vacancies induced any defect levels in the band gap. A defect similar to structure 4 (see Figure 1.7) but with Br and Cs vacancies residing in opposite CsBr planes was found unlikely to form due to the formation energy of 0.67 eV higher than that of structure 4. Pure Br vacancies result in Pb dangling bonds, which introduce defect levels in the band gap close to the conduction band minimum. The authors emphasized that the growth of $CsPbX_3$ under halogen poor conditions should be avoided to minimize the deep defect levels induced by Pb dangling bonds, which are detrimental for the optoelectronic device performance.

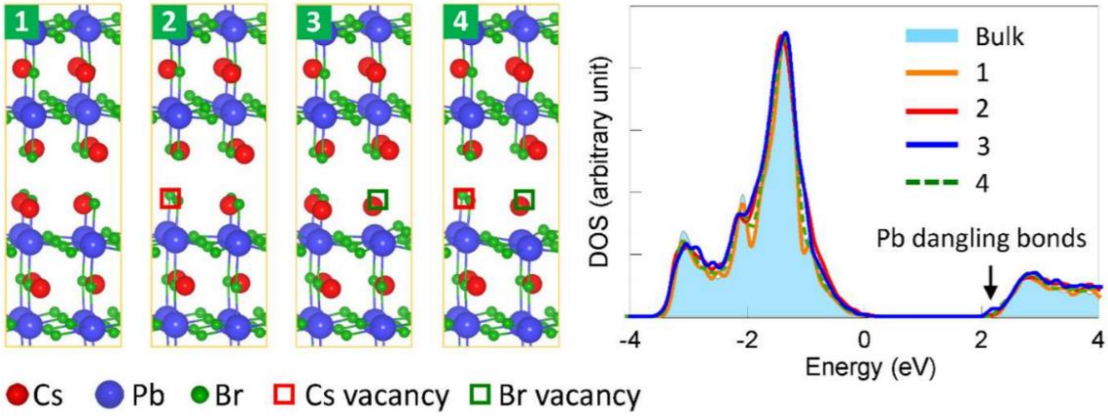

Figure 1.7. Structures and corresponding DOS plots of the RP planar fault with plausible point defects. Structure 1 corresponds to the experimentally observed defect-free RPs. Structures 2, 3 and 4 correspond to the RPs with pure Cs, pure Br and a combination of Cs and Br vacancies, respectively. Arrow in the DOS plot indicates a defect level originating from the Pb dangling bond in structure 3 [12].

The authors also examined the band diagram across the RP fault by performing a layer-by-layer projection of the density of states (LDOS). They found that the RP planar fault was projected to result in considerable band offsets; specifically, positive 134 meV offset for the conduction band and negative 193 offset meV for the valence band. Thus, around room temperature (with a thermal energy of ~26 meV), the RP planar fault is predicted to repel both electrons and holes acting like a semiconductor–insulator–semiconductor junction as shown in Figure 1.8.

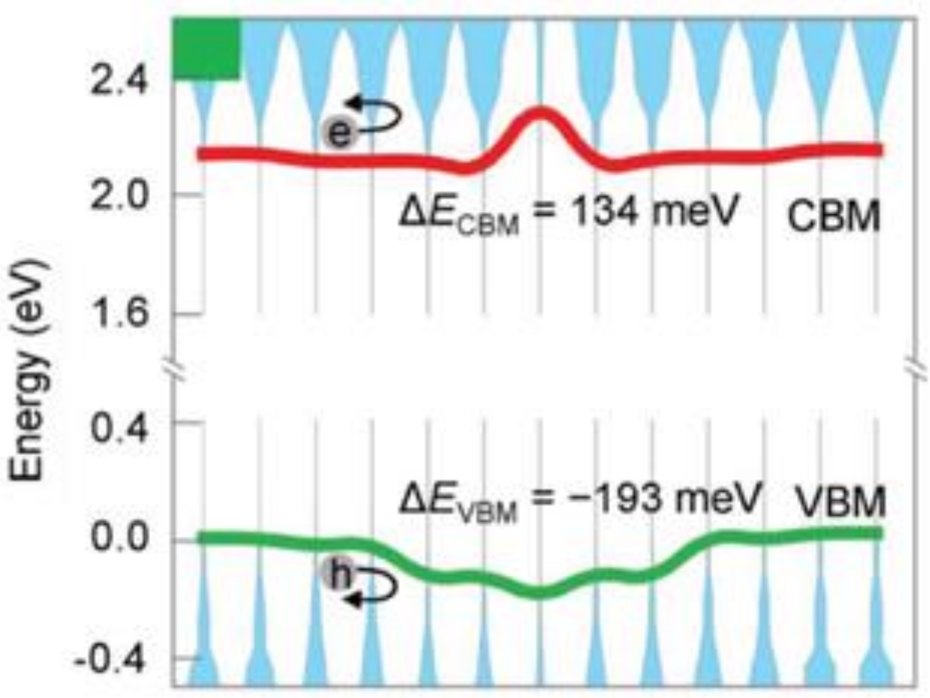

Figure 1.8. DFT-optimized energy band diagram of the RP-$CsPbBr_3$ PNC. The RP fault results in the positive band offset in the conduction band and negative offset in the valence band. The RP fault is projected to repel both electrons and holes [12].

Additionally, the authors performed DFT calculations to examine the macroscopic electrostatic potential (MEP) of electrons across the RP fault. As shown in Figure 1.9, two models with a thickness of 3 and 7 perovskite unit cells indicated that the rock-salt CsBr bilayers exhibited a significantly higher MEP (~1.5 eV) than that of the enclosed perovskite $CsPbBr_3$ domains [9].

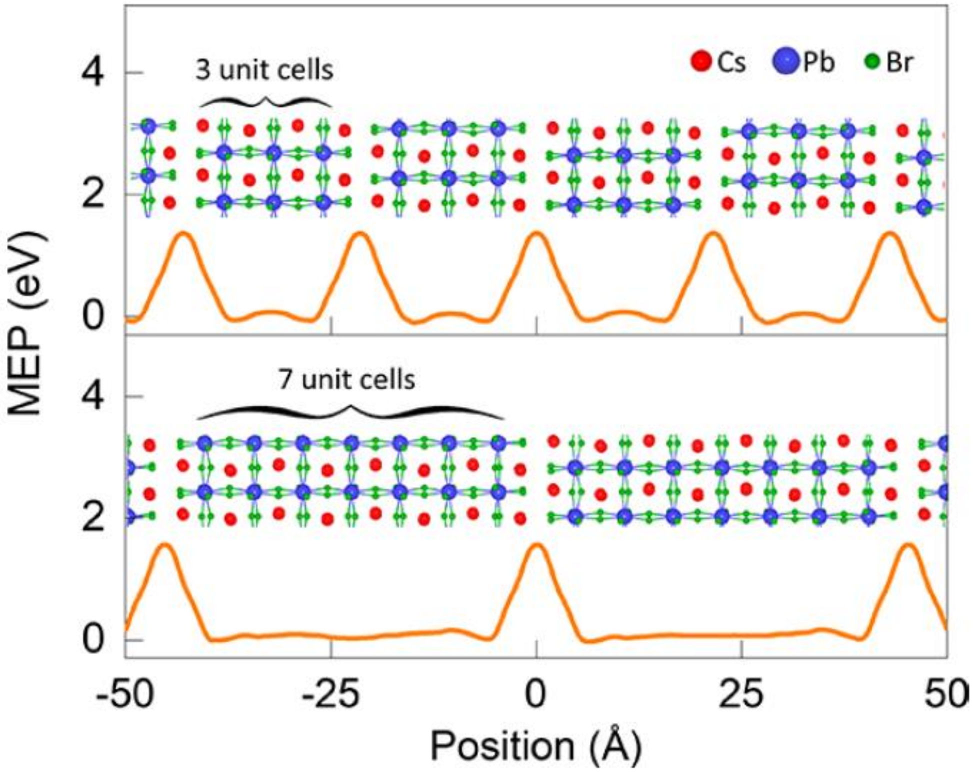

Figure 1.9. DFT-based calculation of the MEP across the RP faults. CsBr bilayers are projected to have 1.5 eV higher MEP than the adjacent perovskite domains with 3 (top) and 7 (bottom) units cells. The RP faults are predicted to result in the formation of built-in quantum wells [9].

These findings allow us to conclude that the RP planar faults in $CsPbBr_3$ PNCs serve as built-in quantum wells which can successfully confine excitons within the perovskite domains, cleaved by the RP faults.

1.5 References

[1] Wells, H. L. Über die Cäsium- und Kalium-Bleihalogenide. *Z. Anorg. Chem.*, **1893**, 3, 195.

[2] Protesescu, L.; Yakunin, S.; Bodnarchuk, M. I.; Krieg, F.; Caputo, R.; Hendon, C. H.; Yang, R.; Walsh, A.; Kovalenko, M. V. Nanocrystals of Cesium Lead Halide Perovskites ($CsPbX_3$, X = Cl, Br, and I): Novel Optoelectronic Materials Showing Bright Emission with Wide Color Gamut. *Nano Lett.* **2015**, *6*, 3692–3696.

[3] He, X.; Qiu, Y.; Yang, S. Fully-inorganic trihalide perovskite nanocrystals: a new research frontier of optoelectronic materials. *Adv. Mater.* **2017**, 29, 1700775.

[4] Zhang, J.; Hodes, G.; Jin, Z.; Liu S. All-Inorganic $CsPbX_3$ Perovskite Solar Cells: Progress and Prospects. *Angew. Chem. Int. Ed.* **2019**, 58, 15596.

[5] Song, J.; Li, J.; Li, X.; Xu, L.; Dong, Y.; Zeng, H. Quantum Dot Light-Emitting Diodes Based on Inorganic Perovskite Cesium Lead Halides ($CsPbX_3$). *Adv. Mater.* **2015**, 27, 7162-7167.

[6] Li, X.; Wu, Y.; Zhang, S.; Cai, B.; Gu, Y.; Song, J.; Zeng, H. $CsPbX_3$ Quantum Dots for Lighting and Displays: Room-Temperature Synthesis, Photoluminescence Superiorities, Underlying Origins and White Light-Emitting Diodes. *Adv. Funct. Mater.* **2016**, 26, 2435-2445.

[7] Kang, J.; Wang, L.W. High Defect Tolerance in Lead Halide Perovskite $CsPbBr_3$. *J. Phys. Chem. Lett.* **2017**, 8, 489−493.

[8] Yu, Y.; Zhang, D.; Yang, P. Ruddlesden–Popper phase in two-dimensional inorganic halide perovskites: a plausible model and the supporting observations. *Nano Lett*. **2017**, 17, 9, 5489-5494

[9] Morrell, M. V.; He, X.; Luo, G.; Thind, A. S.; White, T. A.; Hachtel, J. A.; Borisevich, A. Y.; Idrobo, J. C.; Mishra, R.; Xing, Y. Significantly Enhanced Emission Stability of $CsPbBr_3$ Nanocrystals via Chemically Induced Fusion Growth for Optoelectronic Devices *ACS Appl. Nano Mater*. **2018**, 1, 6091-6098.

[10] Akkerman, Q. A.; Bladt, E.; Petralanda, U.; Dang, Z.; Sartori, E.; Baranov, D.; Abdelhady, A. L.; Infante, I.; Bals, S.; Manna, L. Fully Inorganic Ruddlesden–Popper Double Cl–I and Triple Cl–Br–I Lead Halide Perovskite Nanocrystals. *Chem. Mater.* **2019**, *31*, 2182-2190.

[11] Paul, S.; Bladt, E.; Richter, A. F.; Döblinger, M.; Tong, Y.; Huang, H.; Dey, A.; Bals, S.; Debnath, T.; Polavarapu, L.; Feldmann, J. Manganese-Doping-Induced Quantum Confinement Within Host Perovskite Nanocrystals Through Ruddlesden-Popper Defects. *Angew. Chem. Int. Ed.* **2020**, 59, 6794-6799.

[12] Thind, A. S.; Luo, G.; Hachtel, J. A.; Morrell, M. V.; Cho, S. B.; Borisevich, A. Y.; Idrobo, J.-C.; Xing, Y.; Mishra, R. Atomic Structure and Electrical Activity of Grain Boundaries and Ruddlesden–Popper Faults in Cesium Lead Bromide Perovskite. *Adv. Mater.* **2019**, 31, 1805047.

[13] Ruddlesden, S. N.; Popper, P. New compounds of the K_2NiF_4 type. *Acta Crystallogr.* **1957**, 10, 538−539.

[14] Ruddlesden, S. N.; Popper, P. The compound $Sr_3Ti_2O_7$ and its structure. *Acta Crystallogr.* **1958**, 11, 54–55.

[15] Cava, R. J; Batlogg, B.; Krajewski, J. J.; Farrow, R.; Rupp, A. W. Jr.; White, A. E.; Short, K.; Peck, W. F.;Kometani, T. Superconductivity near 30 K without copper: the $Ba_{0.6}K_{0.4}$ BiO_3 perovskite. *Nature* **1988**, 332, 814-816.

[16] Dwivedi, A.; Cormack, A. N. Crystal chemistry of Ruddlesden-Popper type structures in high T_c ceramic superconductors. *Bull. Mater. Sci.* **1991**, 14, 575−584.

[17] Battle, P. D.; Blundell, S. J.; Green, M. A.; Hayes, W.; Honold, M.; Klehe, A. K.; Laskey, N. S.; Millburn, J. E.; Murphy, L.; Rosseinsky, M. J.; Samarin, N. A.; Singleton, J.; Sluchanko, N. E.; Sullivan, S. P.; Vente, J. F. Colossal magnetoresistance in $Sr_{2-x}Nd_{1+x}Mn_2O_7$ (x = 0.0, 0.1). *J. Phys.: Condens. Matter* **1996**, 8, L427−L434.

[18] Takeguchi, T.; Yamanaka, T.; Takahashi, H.; Watanabe, H.; Kuroki, T.; Nakanishi, H.; Orikasa, Y.; Uchimoto, Y.; Takano, H.; Ohguri, N.; Matsuda, M.; Murota, T.; Uosaki, K.; Ueda, W. Layered Perovskite Oxide: A Reversible Air Electrode for Oxygen Evolution/Reduction in Rechargeable Metal-Air Batteries. *J. Amer. Chem. Soc.* **2013**, 135, 11125–11130.

[19] Pennycook, S. J.; Jesson, D. E. High-resolution Z-contrast imaging of crystals. *Ultramicroscopy* **1991**, 37, 14−38.

[20] Jang, J. H.; Kim, Y. M.; He, Q.; Mishra, R..; Qiao, L.; Biegalski, M. D.; Lupini, A. R.; Pantelides, S. T.; Pennycook, S. J.; Kalinin, S. V.; Borisevich, A. Y. In Situ Observation of Oxygen Vacancy Dynamics and Ordering in the Epitaxial $LaCoO_3$ System. *ACS Nano* **2017**, *11*, 6942.

[21] Gazquez, J.; Guzman, R.; Mishra, R.; Bartolome, E.; Salafranca, J.; Magen, C.; Varela, M.; Coll, M.; Palau, A.; Valvidares, S. M.; Gargiani, P.; Pellegrin, E.; Herrero-Martin, J.; Pennycook, S. J.; Pantelides, S. T.; Puig, T.; Obradors, X. Emerging Diluted Ferromagnetism in High T_c Superconductors Driven by Point Defect Clusters. *Adv. Sci.* **2016**, *3*, 1500295.

[22] Frechero, M. A.; Rocci, M.; Sanchez-Santolino, G.; Kumar, A.; Salafranca, J.; Schmidt, R.; Diaz-Guillen, M. R.; Dura, O. J.; Rivera-Calzada, A.; Mishra, R.; Jesse, S.; Pantelides, S. T.; Kalinin, S. V.; Varela, M.; Pennycook, S. J.; Santamaria, J.; Leon, C. Paving the way to nanoionics: atomic origin of barriers for ionic transport through interfaces. *Sci. Rep.* **2015**, *5*, 17229.

CHAPTER II. ENGINEERING OF RUDDLESDEN-POPPER PLANAR FAULTS IN $CsPbBr_3$ PEROVSKITE NANOCRYSTALS VIA POST-SYNTHETIC FUSION GROWTH

2.1 Abstract

Given recent discovery of the RP phase in $CsPbX_3$ perovskites and very little experimental knowledge on its plausible role in the crystal structure, there is a critical need to research the RP-$CsPbX_3$ PNCs. In this chapter, we explore and provide further support to the mechanism behind the fusion growth of $CsPbBr_3$ PNCs resulting in the formation of RP planar faults. We modify the earlier reported procedure with an attempt to increase the concentration of the developed RP faults. We show that RP-$CsPbBr_3$ PNCs exhibit an outstanding resistance to photodegradation. In addition, we demonstrate that the developed RPs are preserved during the anion-exchange reactions, thus opening the avenue for the future exploration of mixed RP-$CsPb(I/Br)_3$ PNCs.

2.2 Introduction

Since recent discovery, $CsPbX_3$ PNCs have become the staple of the current research in the field of inorganic semiconducting quantum dots. The extensive research was primarily driven by their remarkably bright photoluminescence (PL), exceptionally high PL quantum yield, tunable band gap, and a unique defect-tolerant photophysics [1-8]. $CsPbBr_3$ PNCs stand out among other perovskite halides due to their superior stability [9], and a unique ability for post-synthetic growth [11-12]. In this regard, $CsPbBr_3$ PNCs shall be viewed as a dynamic system that can spontaneously self-assemble into more complex structures.

Udayabhaskararao *et al.* discovered that such spontaneous growth could be triggered by the addition of polar solvents (acetone and ethanol) to $CsPbBr_3$ nanoplatelets [12]. The authors hypothesized that the origin of self-oriented attachment of nanoplatelets was related to the loss of stabilizing ligands from their surfaces.

In pursuing our previous work on post-synthetic growth of $CsPbBr_3$ PNCs [13], we discovered that the growth of $CsPbBr_3$ PNCs was accompanied by the formation of RP planar faults [14] – well known for perovskite oxides, yet not observed in perovskite inorganic halide compounds until then. In light of these findings, we provide new evidence for the proposed reaction path. In addition, we modify the established procedure to vary the concertation of RP faults in $CsPbBr_3$ PNCs. We evaluate the emission stability of $CsPbBr_3$ PNCs with and without RP faults, and explore the anion-exchange reaction in the RP-PNCs.

2.3 Methods

2.3.1 Synthesis of Cs-oleate

Cesium carbonate Cs_2CO_3 (0.407g) was loaded into a 50 ml 3-neck flask along with octadecene (20 mL) and oleic acid (1.25 mL), and dried up in a vacuum for 1 hour at 120°C. The mixture was then heated up to 150°C under nitrogen N_2 atmosphere until all Cs_2CO_3 has reacted with oleic acid.

2.3.2 Synthesis of $CsPbBr_3$ Perovskite Nanocrystals

$CsPbBr_3$ PNCs were synthesized by a hot-injection method, following the procedure of Protesescu *et al.* [1]. Lead bromide $PbBr_2$ (0.069 g) was loaded into a 25 mL 3-neck flask along with octadecene (5 mL) and dried up in a vacuum for 1 hour at 120°C. Oleic acid (0.5 mL) and oleylamine (0.5 mL), used as stabilizing surfactants, were injected at 120°C under nitrogen N_2 atmosphere. After complete solubilization of $PbBr_2$, the mixture was heated to 180°C, and preheated to 100°C Cs-oleate (0.4 mL) was injected. Upon injection, the PNCs growth was quenched with a water-ice bath. Injection at 180°C yields PNCs with an average size of 8 nm.

2.3.3 Purification of $CsPbBr_3$ Perovskite Nanocrystals

Crude PNCs solution was centrifuged at 4000 rpm for 12 minutes. The supernatant was decanted, and the PNCs were redispersed in anhydrous n-heptane. Hereafter this product is referred to $CsPbBr_3$ or non-RP PNCs.

2.3.4 Formation of Ruddlesden-Popper Faults via Fusion Growth

Prior to centrifugation, ethyl acetate was added to the crude PNCs solution, following abovementioned purification procedure. Then 0.2M solution of diethylzinc (DEZ) in anhydrous n-heptane was injected dropwise to $CsPbBr_3$ PNCs in the glovebox under Ar atmosphere at room temperature. As a result, stabilizing surfactants were stripped away, leading to PNCs fusion accompanied by the formation of RP faults. Hereafter the product referred to RP-$CsPbBr_3$ or RP- PNCs. The synthesis, purification and fusion growth steps are illustrated in Scheme 2.1.

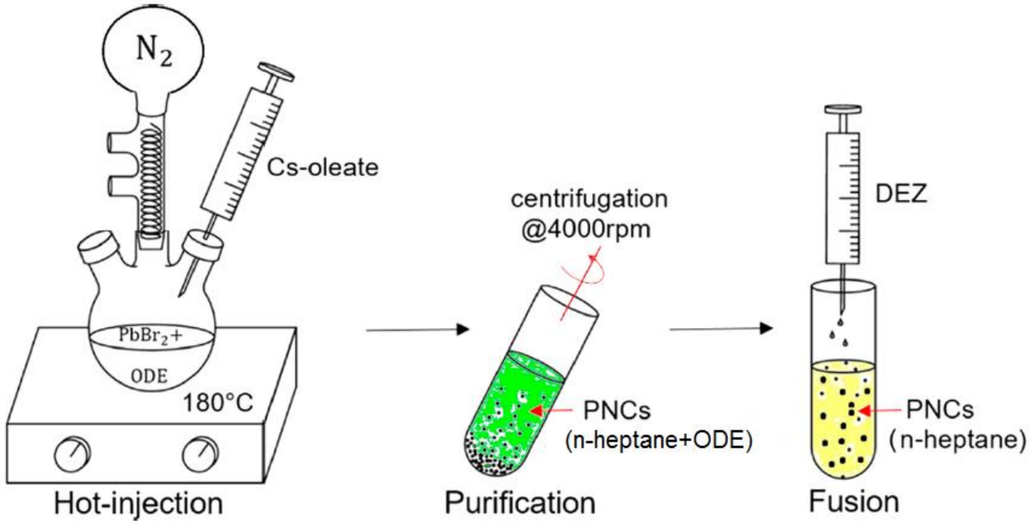

Scheme 2.1. Illustration of the synthesis, purification, and post-synthetic fusion growth steps [14]. Cs-oleate is injected to the mixture of $PbBr_2$, oleic acid and oleylamine in octadecene at 180°C. The reaction is quenched with the ice-water bath, and the mixture is centrifuged at 4000 rpm. The octadecene is then decanted and the PNCs are dissolved in n-heptane. The injection of DEZ results in the removal of stabilizing ligands from the surface of the PNCs and their subsequent fusion, accompanied by the formation of the RP faults.

2.3.5 Anion-exchange reaction

Lead iodide PbI_2 dissolved in octadecene with oleic acid and oleylamine was introduced dropwise to RP-$CsPbBr_3$ PNCs solution. Fast color change from green to red occurred confirming partial substitution of Br with I anions in the perovskite structure.

2.3.6 Characterization methods

Transmission Electron Microscopy imaging were performed on FEI Tecnai F30 Twin 300kV transmission electron microscope.

The Fourier transform Infrared (FTIR) spectroscopy was conducted on a Thermo Nicolet Nexus 4700 FTIR spectrometer.

Photoluminescence (PL) in emission stability experiments was measured with Varian Cary Eclipse fluorescence spectrometer.

Low temperature PL studies were carried in a closed-cycle CTI refrigerator using the 325 nm wavelength of a HeCd laser as the excitation source at a power of <10 mW on the sample; and the PL spectra from drop-casted films were collected using Ocean Optics USB 2000.

2.4 Results and Discussion

2.4.1 Formation of Ruddlesden-Popper Planar Faults in $CsPbBr_3$ Perovskite Nanocrystals via Fusion Growth

In the previous work, we postulated that the growth of $CsPbBr_3$ PNCs occurred due to a vigorous reaction of diethylzinc with the carboxylate ions on the surface of PNCs [13]. For the ease of the readers, the illustration of the proposed reaction path is repeated in the supplemental information (Scheme S2.1). We have performed Fourier transform infrared spectroscopy (FTIR) for both types of PNCs (Fig. 2.1).

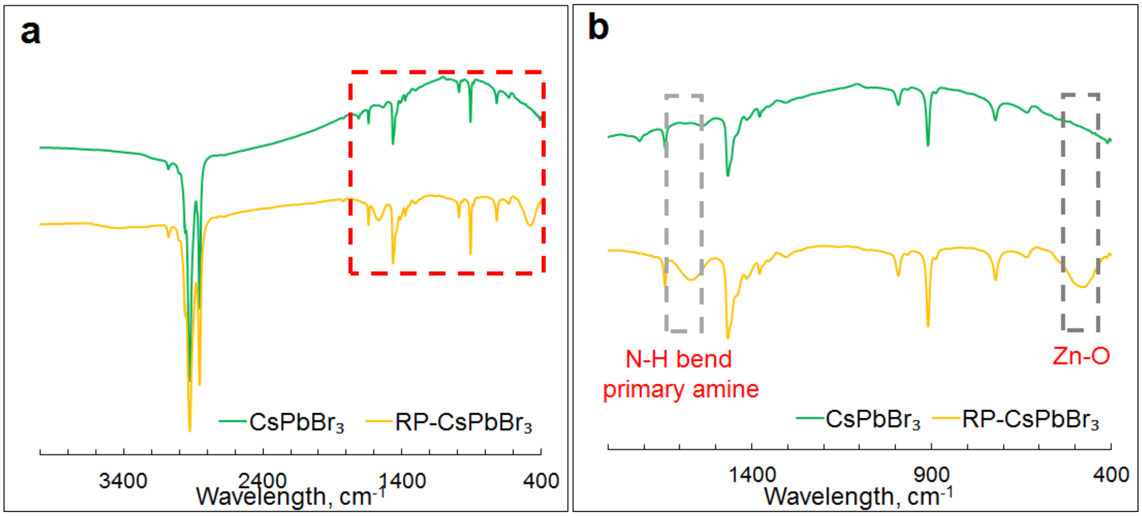

Figure 2.1. (a) FTIR spectra of $CsPbBr_3$ PNCs with (yellow) and without (green) RPs. (b) Enlarged image of the area highlighted in red in panel a. The two peaks in RP-$CsPbBr_3$ PNCs are assigned to Zn-O stretch and primary amine N-H bend [14].

We found that the FTIR spectra are nearly identical, except the two peaks appearing in the RP-$CsPbBr_3$ PNCs at 482 cm^{-1} assigned to Zn−O stretching [15], and at 1566 cm^{-1} assigned to primary amine N−H bending [16]. These findings lend support for the proposed reaction path. Thus, the reaction on the surface depleted stabilizing surface ligands, which subsequently led to the fusion of the PNCs. HAADF STEM images of the produced RP-$CsPbBr_3$ PNCs, a close up image of experimentally observed RP planar faults and their atomic model are delivered in Figure S2.1.

We then proceeded by looking into ways on how to multiply the occurrence of the RP faults in $CsPbBr_3$ PNCs. Since the RP fault is composed of CsBr ions and is formed via process of fusion, then the possibility for developing an RP fault directly depends on $CsPbBr_3$ PNCs available in the solution, and on how many of those are tailored with CsBr planes.

2.4.2 Fusion of $CsPbBr_3$ Perovskite Nanocrystals in the Excess of CsBr

Here, the experimental procedure was modified to enable tailoring of $CsPbBr_3$ PNCs with Cs and Br ions. As such, PNCs were synthesized and purified following established procedure. Then, a drop of saturated solution of CsBr salt in deionized water was introduced into PNCs, and the mixture was left stirred for 1 hour. We take advantage of the high solubility of CsBr in water, and immiscibility of n-heptane with water. We anticipate an ion exchange at the surface contact between the water droplet, saturated with Cs^+ and Br^- ions, and the PNCs dispersed in n-heptane. Thus, if a Cs^+ or Br^- vacancy is present on the surface of $CsPbBr_3$ PNCs, it will likely be 'filled' by Cs^+ or Br^- from the water (Scheme 2.2).

As predicted, the fusion of $CsPbBr_3$ PNCs in the excess of CsBr indeed resulted in higher occurrence of RP faults (Figure 2.2, S2.2).

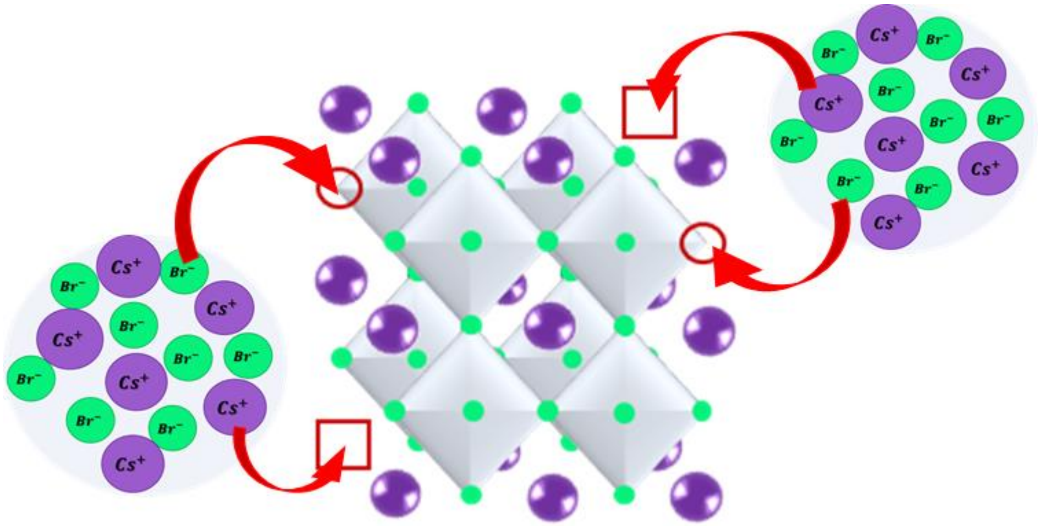

Scheme 2.2. Illustration of the Cs and Br ion exchange at the interface of the water drop saturated with CsBr salt and the $CsPbBr_3$ PNC in heptane. If Cs^+ or Br^- vacancies occur (red square or a circle, respectively), they will likely be filled with Cs^+ or Br^- ions from the water drop.

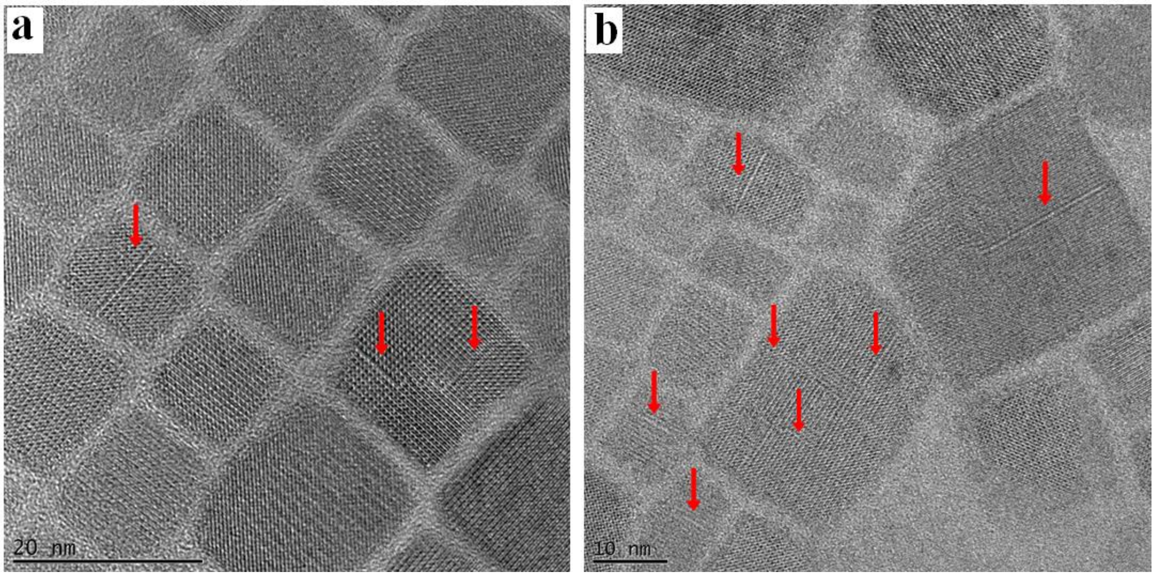

Figure 2.2. TEM images of the RP-$CsPbBr_3$ PNCs formed via (a) standard procedure and (b) in the excess of CsBr. The RP-$CsPbBr_3$ PNCs produced in the excess of CsBr displayed higher occurrence of RP planar faults. The RPs are highlighted with red arrows.

Additionally, we also observed continuous growth of RP-PNCs in colloids, accompanied by the formation of an extensive network out of RP faults (Fig. 2.3)

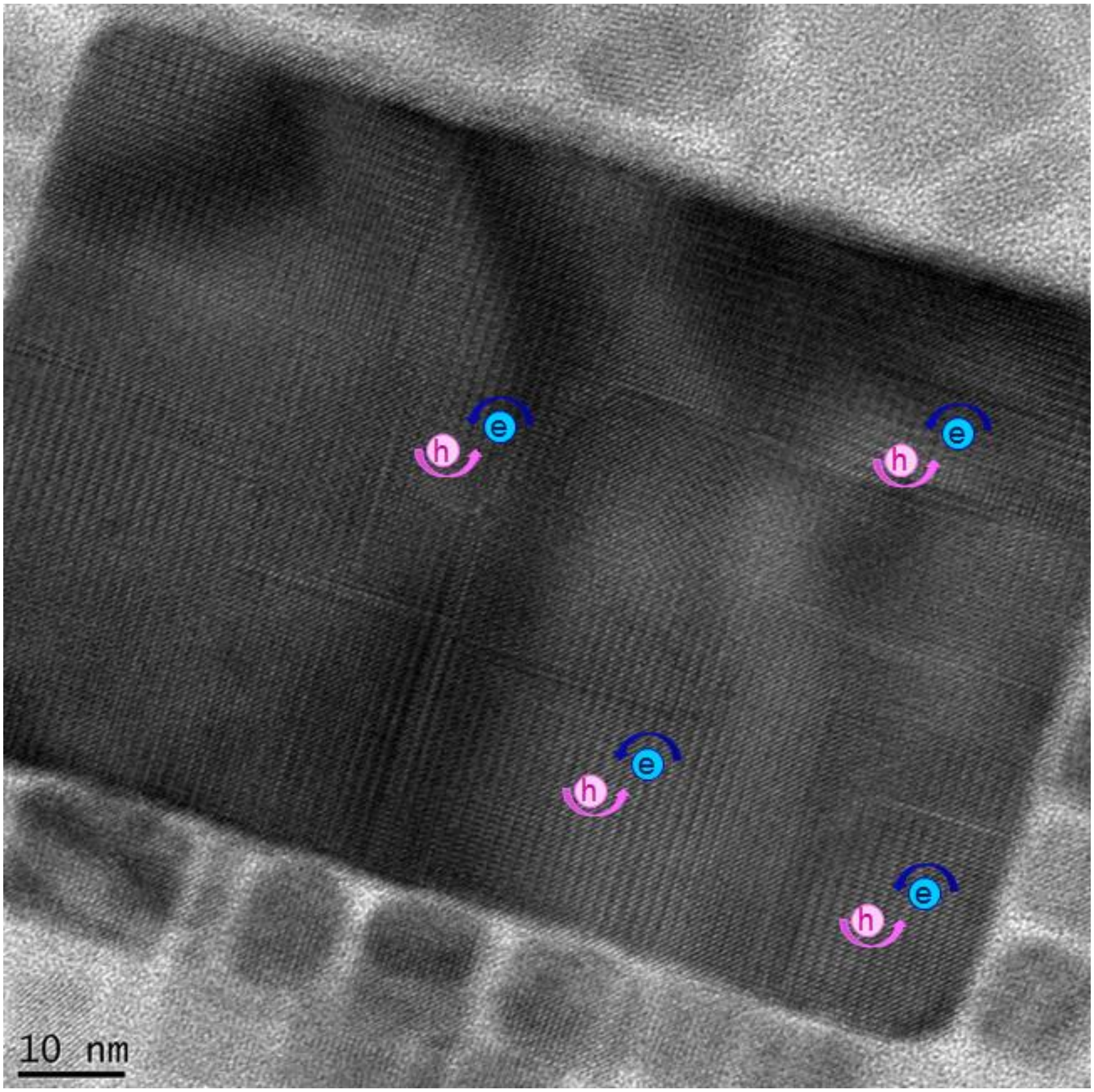

Figure 2.3. TEM image displaying the RP-$CsPbBr_3$ PNC with an extensive network of RP faults. The RPs are predicted to confine excitons in the enclosed perovskite domains.

Given the ionic nature of the PNCs and the reduced amount of stabilizing ligands on the surface, we postulated that the growth with time occurred via Ostwald ripening [17]. The growth of PNCs is facilitated due to the increased moisture level, introduced with water, known to assist in PNCs agglomeration [18]. However, the lateral overall size in RP-$CsPbBr_3$ PNC becomes irrelevant due to retaining of the quantum confinement in the perovskite domains, cleaved by RPs.The effective Bohr diameter for $CsPbBr_3$ PNCs was originally estimated to be ∼7 nm [1]. Yet, most recent work on the absorption and emission properties of $CsPbBr_3$ PNCs reported the presence of quantum confinement effect in the PNCs up to 16 nm in size [19]. Therefore, as long as the size of the perovskite domains, cleaved by the RPs, is within the exciton Bohr diameter, quantum confinement will be preserved [20], if not enhanced by the presence of the insulating RPs [14].

2.4.3 Emission Stability of $CsPbBr_3$ Perovskite Nanocrystals with and without Ruddlesden-Popper Planar Faults

The stability of PL emission of RP-$CsPbBr_3$ PNCs produced by both procedures was studied, and compared to the stability of PNCs without the RPs. Colloid samples of RP and non-RP PNCs, equally dispersed in n-heptane, were exposed to a continuous light source at 400 nm for 60 min (45 mins in case of fusion with CsBr excess). Measurements were then taken with a 1 min interval. RP-$CsPbBr_3$ PNCs, produced with standard fusion procedure, exhibited an extraordinary resistance to photodegradation, displaying rather insignificant (~8%) drop in PL intensity compared to a drastic decrease in PL (93.0%) in non-RP PNCs within 1 h (Fig. 2.4a).

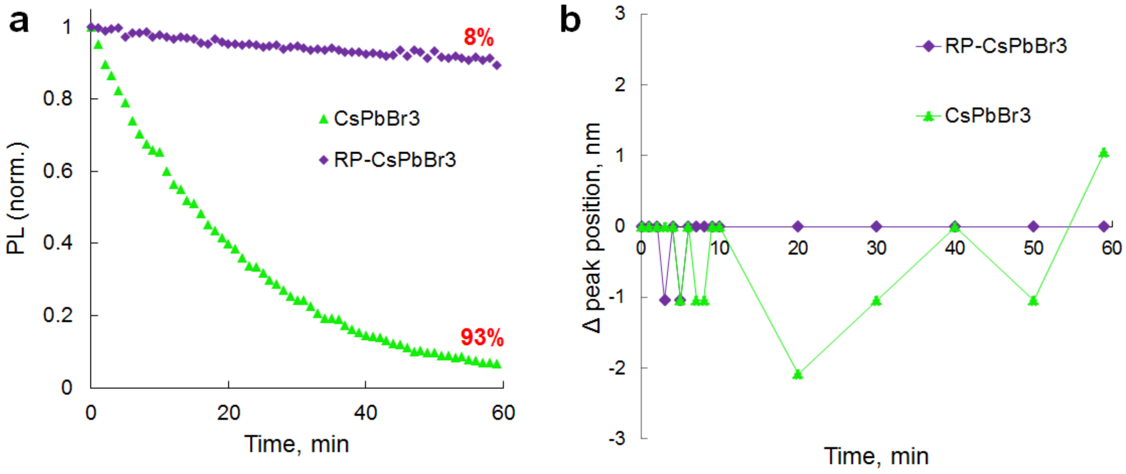

Figure 2.4. (a) Normalized PL intensity dynamics of with (purple) and without (green) RPs upon continuous light exposure at 400 nm. RP-$CsPbBr_3$ PNCs displayed an extraordinary resilience to photodegradation with an 8% loss in PL intensity upon 1 hour, compared to 93% in non-RP PNCs [21]. (b) Change in maximum PL peak position corresponding to data in panel a.

It is common for semiconductor nanocrystals to display fast quenching in the PL intensity with time [21]. A decrease in PL intensity was associated with the formation of quenching surface states due to chemical oxidation, photo-oxidation, or corrosion [22]. It was shown that $CsPbBr_3$ PNCs tend to aggregate when exposed to light, and the formation of such aggregates is accompanied by the development of charge trap sites [23, 24]. Interestingly, we did not observe such aggregation in our experiments upon continuous light exposure of PNCs for 1 h (Fig. 2.4b). On the contrary, we observed an exceptional PL stability in RP-$CsPbBr_3$ PNCs developed via standard fusion procedure. We then studied the PL dynamics in RP-$CsPbBr_3$ PNCs formed in the excess of CsBr. Despite a significantly higher content of RP faults, RP-$CsPbBr_3$ PNCs displayed a 4.6 times faster PL decay within 45 mins compared to the RP-PNCs formed via standard fusion procedure (Fig. 2.5).

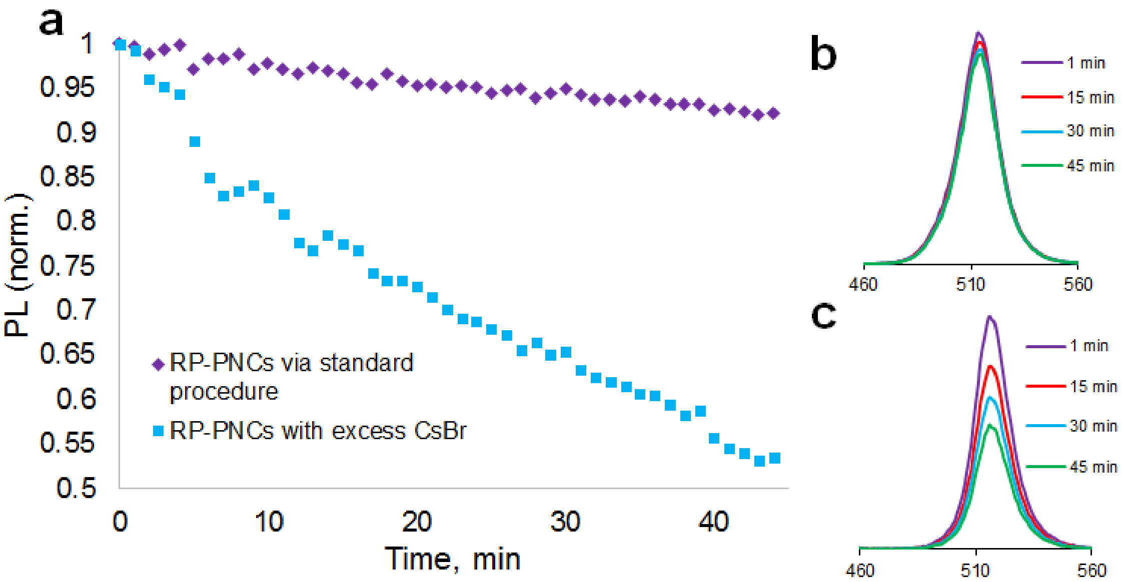

Figure 2.5. (a) Comparison of the PL intensity dynamics of RP-$CsPbBr_3$ PNCs produced via standard procedure (purple) and in the excess of CsBr (blue). The PL decay of the latter is facilitated by the higher moisture content in the solution. Raw data of the PL decay for (b) standard procedure and (c) the excess of CsBr. Curves in panels b and c correspond to measurements taken at 1, 15, 30, and 45 min.

The accelerated PL quenching was attributed to the increased moisture level in the solution introduced with the excess of CsBr. Given the loss in emission properties, the RP-PNCs produced via standard fusion procedure were chosen for all other experiments.

The phenomena of the enhanced stability was reported earlier for hybrid 2D and quasi-2D RP-perovskites, where the insertion of organic layers into the perovskite structure, resulted in the improved stability [25]. The observed enhancement was attributed to the hydrophobic nature of the organic spacers, which effectively shield perovskite layers from moisture. Given the hydrophilic nature of CsBr, such explanation cannot be applied to our case. Yet, since the enhancement in emission stability is only observed in PNCs with PPs, we postulate that it is related to the presence of RPs in the crystal structure.

2.4.4 Quantum Yield of $CsPbBr_3$ PNCs with and without Ruddlesden-Popper Faults

The loss of stabilizing ligands from the surface of the PNCs is often accompanied by a drop in PLQY due to the exposed surface states. The latter may serve as the trap cites, which are capable of capturing the excitons and leading to their non-radiative recombination. Given the remarkable PL emission stability in RP-PNCs despite the loss of ligands, we measured their PLQY and compared it to the non-RP sample. Both types of PNCs were evenly dispersed in n-heptane with absorbance much lower than 0.1 to prevent nonradiative Förster resonance energy transfers [26]. Rhodamine 6G dispersed in ethanol was used as a reference dye. The measurements were taken at 350 nm. QY was estimated using the following formula [27]:

$$\phi = \frac{n^2}{n_0^2}\frac{\alpha A_0}{\alpha_0 A}\phi_0, \tag{2.1}$$

where n is the refractive index of the solvent used, α the absorbance at the excitation wavelength, the area under the emission curve, and ϕ quantum yield. Subscript 0 stands for the reference dye. Remarkably, the QY for RP-$CsPbBr_3$ was estimated to be 11% higher that the non-RP, reaching 77% for the best sample. Non-RP $CsPbBr_3$ PNCs, due to a smaller size, possess higher relative surface area and thus, a higher density of surface states, which can serve as exciton quenchers. Whereas RP-$CsPbBr_3$ PNCs, being larger, have smaller relative surface area. Yet, non-RP PNCs are heavily passivated with organic surfactants, in contrast to RP-PNCs with largely reduced ligands on their surface. Thus, it is reasonable to suggest that higher QY may stem from the presence of the RPs and their ability to serve as built-in quantum wells, suggested by the DFT-based calculations.

2.4.5 Anion-Exchange Reaction in $CsPbBr_3$ Perovskite Nanocrystals with Ruddlesden-Popper Planar Faults

$CsPbX_3$ PNCs possess a unique ability to undergo the anion-exchange reaction [2]. The introduction of PbI_2 or $PbCl_2$ into $CsPbBr_3$ PNCs leads to an immediate partial substitution of Br ions with I or Cl, respectively. This results in the formation of mixed PNCs, accompanied by the subsequent changes in the energy band gap – reduction in case of Cl, and increase in case of I. We were interested in finding out whether RP-$CsPbBr_3$ PNCs would be able to undergo such anion-exchange reaction, and whether RP faults would be preserved during the exchange.

Once PbI_2, the source of I anions, was introduced into RP-PNCs solution, color change of the solution from green to red signified that the anion-exchange occurred. As such the I anions have replaced some of the Br ions in the perovskite structure, resulting in the formation of mixed $CsPb(Br/I)_3$ PNCs.

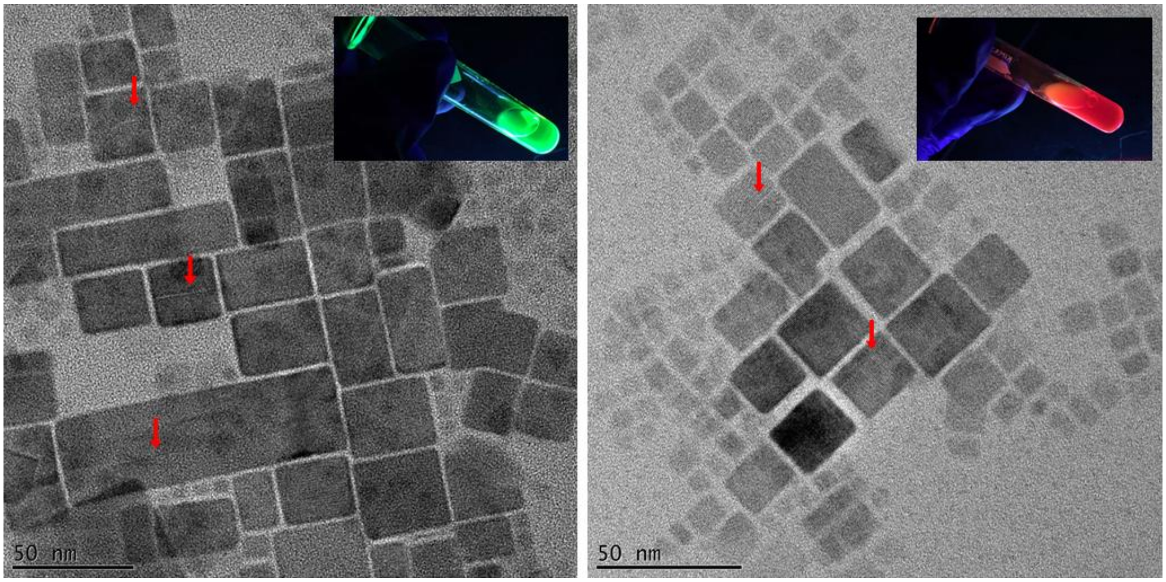

Figure 2.6. TEM images of the RP-$CsPbBr_3$ PNCs before (left) and after (right) anion-exchange reaction. Insets show photos of the colloid samples taken under UV light. RPs are highlighted with red arrows.

Mixed PNCs were then analyzed with the TEM to determine whether RP faults remained during the procedure. Images revealed distinct RP planar faults in both samples - before and after anion-exchange (Fig. 2.6). Though we can positively indicate that the RPs endure the anion-exchange reaction, atomic resolution HAADF STEM imaging is required to determine whether anion-exchange takes place solely in the perovskite domains or at the RP interface as well. To our knowledge, this is the first demonstration of mixed $CsPb(I/Br)_3$ PNCs with the RP faults.

2.4.6 Photoluminescence as a Function of Temperature in $CsPbBr_3$ Perovskite Nanocrystals with and without Ruddlesden-Popper Planar Faults

In collaboration with the group of Professor Suchi Guha, we studied PL response from both type of PNCs as a function of temperature [28]. As seen in Figure 2.7, there is rather insignificant change in the PL peak position (within ±2 nm) for both samples in the temperature range of 60-300 K.

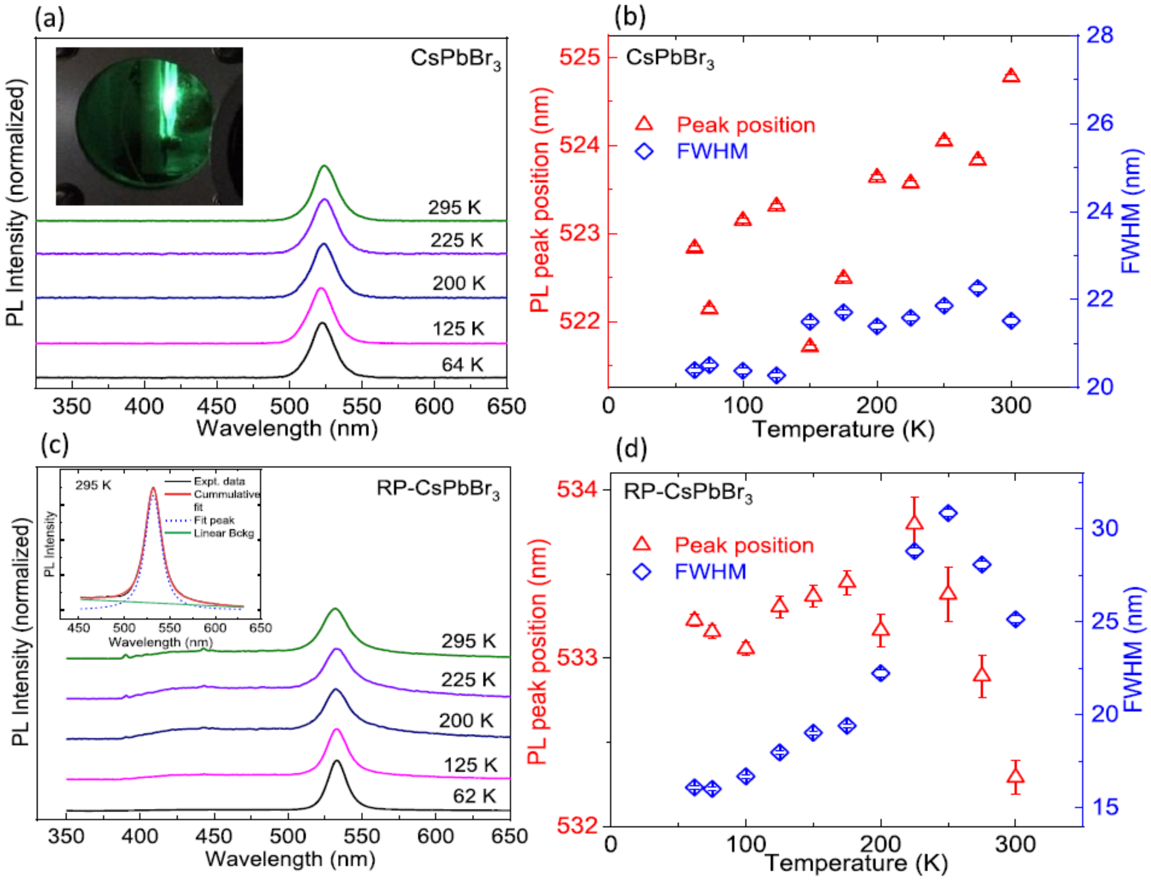

Figure 2.7. PL spectra of (a) non-RP and (c) RP-$CsPbBr_3$ PNCs at selected temperatures. Corresponding temperature dependence of PL peak position and full width at half-maximum (FWHM) of non-RP (b) and (d) RP-$CsPbBr_3$ PNCs [28].

These results are consistent with a homogeneous particle size distribution along with quantum confinement effects in both samples. However, some differences are observed between non-RP and RP-$CsPbBr_3$ PNCs. Except for an anomaly in the peak position at ~200 K, the overall trend in $CsPbBr_3$ is a red shift in PL energies with increasing temperature (note that the PL peak positions are plotted in nm and not in eV). The red shift in energy with temperature is typical of quantum wells and bulk semiconductors due to a renormalization of band energies by electron−phonon interactions [29]. In semiconducting quantum dots, however, depending on the size distribution, the PL energies often blue-shift due to a loss of carriers from the larger quantum dots that have lower energies to the smaller quantum dots with higher energies [30]. Furthermore, recent Raman scattering study from $CsPbBr_3$ PNCs as a function of temperature shows an order-disorder transition around 200 K [31]. Therefore, the observed anomaly in the PL at ~200 K could be related to this transition.

The PL energy in RP-$CsPbBr_3$ PNCs remains almost unchanged till 250 K, beyond which there is a slight blue shift (of ~7 meV between 250 and 300 K). The origin of this shift is not clear, although it is conceivable that it is a signature of a phase transition.

2.5 Conclusions

In summary, we demonstrated that the post-synthetic fusion growth of $CsPbBr_3$ PNCs was accompanied by the formation of RP planar faults. By modifying the procedure, we showed that the fusion growth in the excess of CsBr increased the occurrence of RPs in the PNCs. We found that in the absence of high moisture content RP-$CsPbBr_3$ PNCs possessed exceptionally higher resistance to photodegradation compared to the non-RP PNCs. For the first time, we demonstrate mixed $CsPb(I/Br)_3$ PNCs with RP planar faults produced via successful anion-exchange reaction in RP-$CsPbBr_3$ PNCs.

2.6 Acknowledgements

We would like to thank Dr. Peter V. Cornish for providing free access to the optical equipment for emission stability study. We recognize assistance and support from Dr. Tommi White and Dr. Xiaoqing He in obtaining TEM images. We express gratitude to Dr Guha and Dr Yesudhas for their major contribution in the studies of the PL as a function of temperature. We thank Kristina Moore for the input in drawing Scheme 2.1.

2.7 Supplemental Information

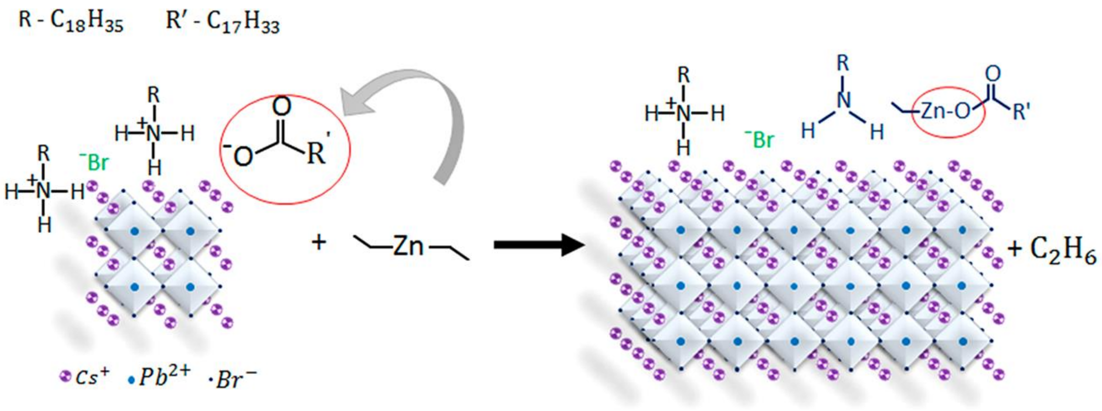

Scheme S2.1. Schematic illustration of the reaction path for diethylzinc with carboxylates on the surface of $CsPbBr_3$ PNCs. Upon dissociation, diethylzinc reacts with the carboxylate anion forming C_2H_5−Zn−OOR′ compound; oleylammonium cation donates hydrogen atom to the remaining ethyl group to produce ethane. Both C_2H_5−Zn−OOR′ and oleylamine leave the surface of nanocrystals due to the loss of ionic bonding. The removal of the stabilizing ligands from the surface of the PNCs results in their fusion, accompanied by the formation of RPs [14].

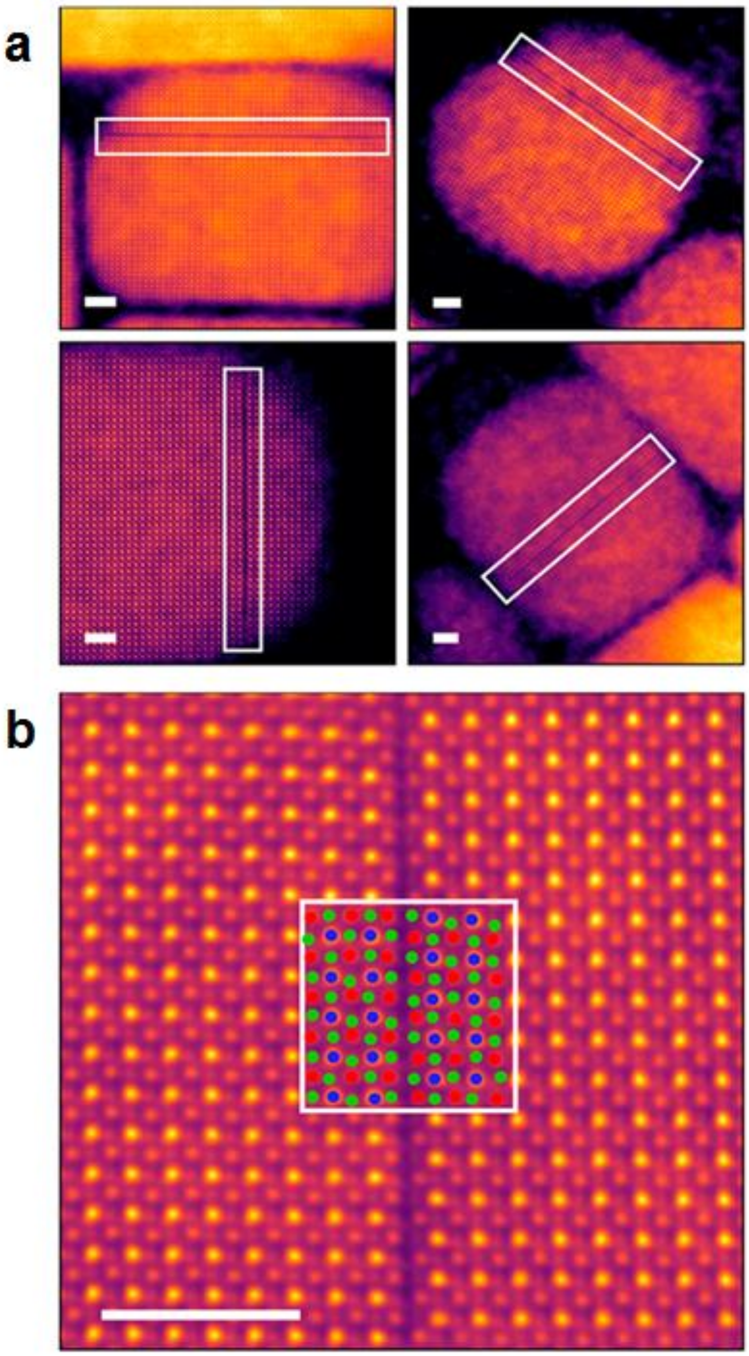

Figure S2.1. (a) Composite of low-magnification HAADF images showing RP planar faults (highlighted as rectangular boxes) in several of the RP-CsPbBr$_3$ PNCs. (b) Atomic resolution HAADF image of a RP planar fault with an overlaid atomic model. The blue, red, and green atomic columns correspond to Pb, Cs, and Br, respectively. The scale bars correspond to 3 nm [14].

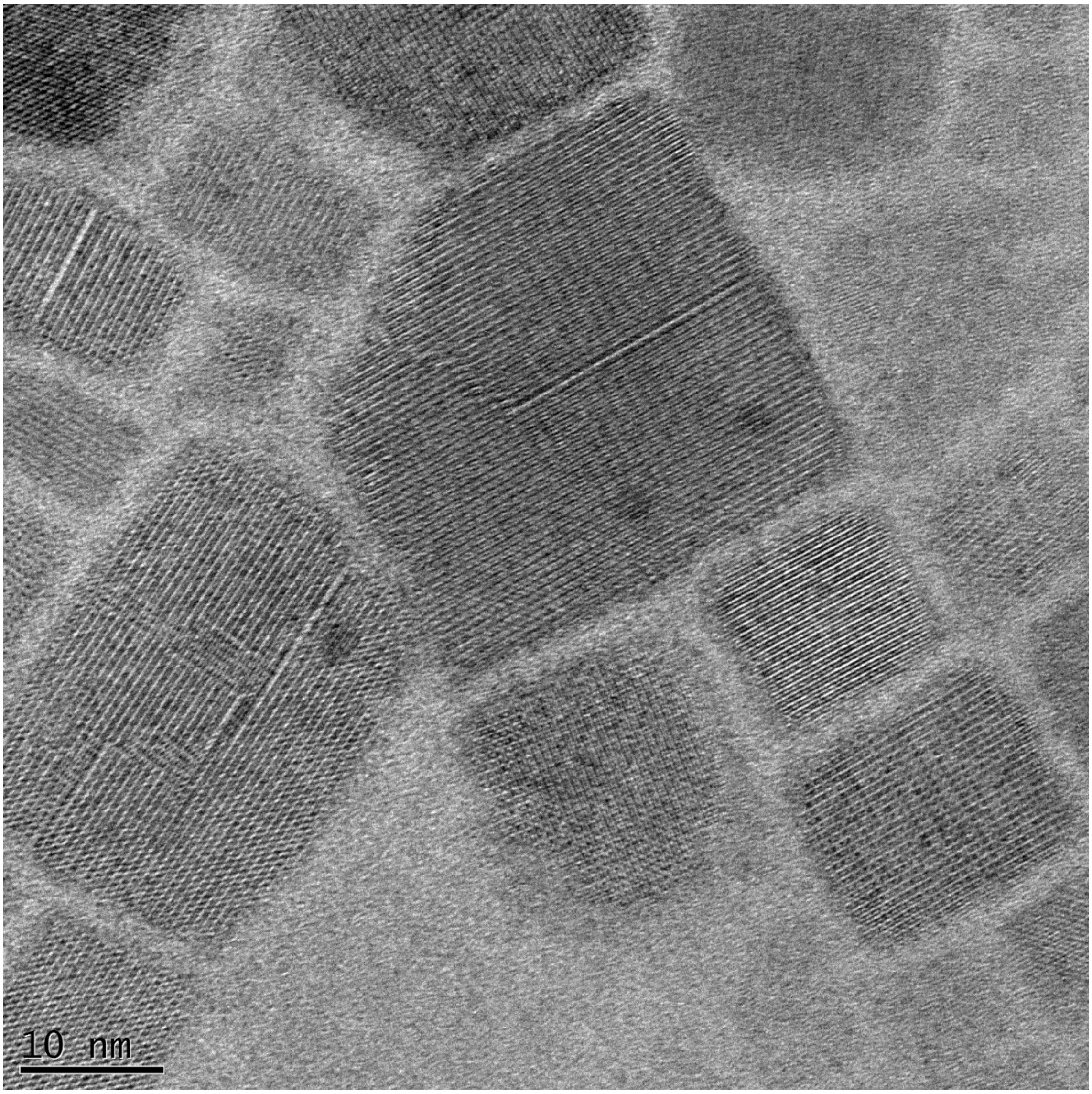

Figure S2.2. High-resolution TEM image displaying multiple RP planar faults formed via fusion growth of $CsPBBr_3$ PNCs in the excess of CsBr.

2.8 References

[1] Protesescu, L.; Yakunin, S.; Bodnarchuk, M. I.; Krieg, F.; Caputo, R.; Hendon, C. H.; Yang, R.; Walsh, A.; Kovalenko, M. V. Nanocrystals of Cesium Lead Halide Perovskites ($CsPbX_3$, X = Cl, Br, and I): Novel Optoelectronic Materials Showing Bright Emission with Wide Color Gamut. *Nano Lett.* **2015**, *6*, 3692–3696.

[2] Nedelcu, G.; Protesescu, L.; Yakunin, S.; Bodnarchuk, M. I.; Grotevent, M. J.; Kovalenko, M. V. Fast Anion-Exchange in Highly Luminescent Nanocrystals of Cesium Lead Halide Perovskites (CsPbX3, X = Cl, Br, I). *Nano Lett.* **2015**, 15, 5635−5640.

[3] He, X.; Qiu, Y.; Yang, S. Fully-inorganic trihalide perovskite nanocrystals: a new research frontier of optoelectronic materials. *Adv. Mater.* **2017**, 29, 1700775.

[4] Huang, H.; Polavarapu, L.; Sichert, J. A.; Susha, A. S.; Urban, A. S.; Rogach, A. L. Colloidal Lead Halide Perovskite Nanocrystals: Synthesis, Optical Properties and Applications. *NPG Asia Mater*. **2016**, *8*, e328.

[5] Li, X.; Wu, Y.; Zhang, S.; Cai, B.; Gu, Y.; Song, J.; Zeng, H. $CsPbX_3$ Quantum Dots for Lighting and Displays: Room-Temperature Synthesis, Photoluminescence Superiorities, Underlying Origins and White Light-Emitting Diodes. *Adv. Funct. Mater.* **2016**, 26, 2435-2445.

[6] Lang, L.; Yang, J.-H.; Liu, H.-R.; Xiang, H. J.; Gong, X. G. First-principles study on the electronic and optical properties of cubic ABX_3 halide perovskites. *Phys. Lett. A* **2014**, *378*, 290-293.

[7] Kang, J.; Wang, L.W. High Defect Tolerance in Lead Halide Perovskite $CsPbBr_3$. *J. Phys. Chem. Lett.* **2017**, 8, 489−493.

[8] Huang, H.; Bodnarchuk, M. I.; Kershaw, S. V.; Kovalenko, M. V.; Rogach, A. L. Lead Halide Perovskite Nanocrystals in the Research Spotlight: Stability and Defect Tolerance. *ACS Energy Lett* **2017,** *2* (9), 2071-2083.

[9] Kulbak, M.; Cahen, D.; Hodes, G. How Important Is the Organic Part of Lead Halide Perovskite Photovoltaic Cells? Efficient CsPbBr3 Cells. *J. Phys. Chem. Lett*. **2015**, *6*, 2452−2456.

[10] Bekenstein, Y.; Koscher, B. A.; Eaton, S. W.; Yang, P.; Alivisatos, A. P. Highly Luminescent Colloidal Nanoplates of Perovskite Cesium Lead Halide and Their Oriented Assemblies. *J. Am. Chem. Soc.* **2015**, *137*, 16008–16011.

[11] Vybornyi, O.; Yakunin, S.; Kovalenko, M. V. Polar-solvent-free colloidal synthesis of highly luminescent alkylammonium lead halide perovskite nanocrystals. *Nanoscale* **2016**, *8*, 6278-6283.

[12] Udayabhaskararao, T.; Kazes, M.; Houben, L.; Lin, H.; Oron, D. Nucleation, growth, and structural transformations of perovskite nanocrystals. *Chem. Mater.* **2017**, *29*, 1302–1308.

[13] Goriacheva, M. (2017). Chemically-induced controlled growth of $CsPbBr_3$ perovskite nanocrystals. [Master's thesis, University of Missouri – Columbia]. MOSpace. https://hdl.handle.net/10355/66737

[14] Morrell, M. V.; He, X.; Luo, G.; Thind, A. S.; White, T. A.; Hachtel, J. A.; Borisevich, A. Y.; Idrobo, J. C.; Mishra, R.; Xing, Y. Significantly Enhanced Emission Stability of $CsPbBr_3$ Nanocrystals via Chemically Induced Fusion Growth for Optoelectronic Devices *ACS Appl. Nano Mater*. **2018**, 1, 6091-6098.

[15] Lavand, A. B.; Malghe, Y. S. Synthesis, characterization and visible light photocatalytic activity of nitrogen-doped zinc oxide nanospheres. *J. Asian Ceramic Soc.* **2015**, 3, 305−310.

[16] Pan, A.; He, B.; Fan, X.; Liu, Z.; Urban, J. J.; Alivisatos, A. P.; He, L.; Liu, Y. Insight into the Ligand-Mediated Synthesis of Colloidal $CsPbBr_3$ Perovskite Nanocrystals: The Role of Organic Acid, Base, and Cesium Precursors. *ACS Nano* **2016**, 10, 7943−7954.

[17] Ostwald, W. Studien über die Bildung und Umwandlung fester Körper. *Zeitschrift für Physikalische Chemie* **1897**, 22, 289–330.

[18] Gomez, L.; Lin, J.; Weerd, C.; Poirier, L.; Boehme, S. C.; von Hauff, E.; Fujiwara, Y.; Suenaga, K.; Gregorkiewicz, T. Extraordinary Interfacial Stitching between Single All-Inorganic Perovskite Nanocrystals. *ACS Appl. Mater. Interfaces* **2018**, *10*, 5984-5991.

[19] Becker, M. A.; Vaxenburg, R.; Nedelcu, G.; Sercel, P. C.; Shabaev, A.; Mehl, M. J.; Michopoulos, J. G.; Lambrakos, S. G.; Bernstein, N.; Lyons, J. L.; Stöferle, T.; Mahrt, R. F.; Kovalenko, M. V.; Norris, D. J.; Rainò, G.; Efros, A. L. Bright triplet excitons in caesium lead halide perovskites. *Nature* **2018**, 553, 189−194.

[20] Smith, A. M.; Nie, S. Semiconductor Nanocrystals: Structure, Properties, and Band Gap Engineering. *Acc. Chem. Res.* **2010**, 43, 190−200.

[21] Kagan, C. R.; Murray, C. B.; Nirmal, M.; Bawendi, M. G. Electronic energy transfer in CdSe quantum dot solids. *Phys. Rev. Lett.* **1996**, 76, 1517−1520.

[22] Malak, S. T.; Yoon, Y. J.; Smith, M. J.; Lin, C. H.; Jung, J.; Lin, Z.; Tsukruk, V. V. Decay-to-Recovery Behavior and on−off Recovery of Photoluminescence Intensity from Core/Shell Quantum Dots. *ACS Photonics* **2017**, 4, 1691−1704.

[23] Huang, S.; Li, Z.; Wang, B.; Zhu, N.; Zhang, C.; Kong, L.; Zhang, Q.; Shan, A.; Li, L. Morphology Evolution and Degradation of $CsPbBr_3$ Nanocrystals under Blue Light-Emitting Diode Illumination. *ACS Appl. Mater. Interfaces* **2017**, 9, 7249−7258.

[24] Chen, J.; Liu, D.; Al-Marri, M. J.; Nuuttila, L.; Lehtivuori, H.; Zheng, K. Photo-stability of $CsPbBr_3$ perovskite quantum dots for optoelectronic application. *Sci. China Mater.* **2016**, 59, 719−727.

[25] Chen, Z.; Guo, Y.; Wertz, E.; Shi, J. Merits and Challenges of Ruddlesden-Popper Soft Halide Perovskites on Electro-Optics and Optoelectronics. *Adv Mater.* **2018**, 31, 1, 1803514.

[26] Kagan, C. R.; Murray, C. B.; Nirmal, M.; Bawendi, M. G. Electronic energy transfer in CdSe quantum dot solids. *Phys. Rev. Lett.* **1996**, 76, 1517−1520.

[27] Williams, A. T. R.; Winfield, S. A.; Miller, J. N. Relative fluorescence quantum yields using a computer-controlled luminescence spectrometer. *Analyst* **1983**, 108, 1067−1071.

[28] Yesudhas, S.; Morrell, M. V.; Anderson, M. J.; Ullrich, C.A.; Kenney-Benson, C.; Xing, Y.; Guha, S. Pressure-Induced Phase Changes in Cesium Lead Bromide Perovskite Nanocrystals with and without Ruddlesden−Popper Faults. *Chem. Mater.* **2020**, 32, 785−794.

[29] Guha, S.; Cai, Q.; Chandrasekhar, M.; Chandrasekhar, H. R.; Kim, H.; Alvarenga, A. D.; Vogelgesang, R.; Ramdas, A. K.; Melloch, M. R. Photoluminescence of short-period GaAs/AlAs superlattices: A hydrostatic pressure and temperature study. *Phys. Rev. B* **1998**, 58, 7222−7229.

[30] Brown, J.; Elsass, C.; Poblenz, C.; Petroff, P. M.; Speck, I. S. Temperature Dependent Photoluminescence of MBE Grown Gallium Nitride Quantum Dots. Phys. Status Solidi B 2001, 228, 199−202.

[31] Liao, M.; Shan, B.; Li, M. In Situ Raman Spectroscopic Studies of Thermal Stability of All-Inorganic Cesium Lead Halide ($CsPbX_3$, X= Cl, Br, I) Perovskite Nanocrystals. *J. Phys. Chem. Lett.* **2019**, 10, 1217−1225.

CHAPTER III. OPTOELECTRONIC PROPERTIES OF $CsPbBr_3$ PEROVSKITE NANOCRYSTALS WITH AND WITHOUT RUDDLESDEN-POPPER PLANAR FAULTS

3.1 Abstract

While the layered hybrid RP-halide perovskites have already established themselves as the frontrunners among the candidates in optoelectronics, their all-inorganic counterparts remain least explored in the RP-type perovskite family. Herein, we study and compare the optoelectronic properties of all-inorganic $CsPbBr_3$ PNCs with and without RP planar faults. We find that the RP-$CsPbBr_3$ PNCs possess both higher exciton binding energy and longer exciton lifetimes. The former is ascribed to a quantum confinement effect in the PNCs induced by the RP faults. The latter is attributed to a spatial electron-hole separation across the RP faults. A striking difference is found in the up-conversion photoluminescence response in the two types of the $CsPbBr_3$ PNCs**.**

3.2 Introduction

A family of RP-halide perovskites stands out among other perovskite compounds due to their unique crystalline structure, in which the ABX_3 perovskite layers are interleaved with AX rock-salt type layers, forming an RP phase [1, 2]. The RP phase was suggested to contribute to a number of intriguing properties in perovskite oxides, including high T_c superconductivity, colossal magnetoresistance, and ferroelectricity [3-6]. In light of the rapid development in the hybrid halide perovskites in photovoltaics, much attention has been focused on hybrid 2D or quasi-2D RP, or layered perovskites, in which the perovskite slabs, serving as quantum wells, are separated by insulating organic spacers, acting as potential barriers [7]. Within a short period, layered 2D halide perovskites have established themselves as excellent candidates for highly efficient and stable solar cells and light emitting devices (LEDs) [8-12]. Owing to their hydrophobic nature, organic spacers effectively shield perovskite layers from moisture – a major stability hurdle in the perovskite-based technology. However, the organic spacers, due to their insulating nature, can induce charge accumulation, impede electron transport, and lead to non-radiative recombination losses [13]. Efforts have been made by reducing the length of organic spacers, or implementing all-inorganic RP perovskite nanocrystals with naturally occurring ultrathin RP planar faults.

The existence of the RP phase in all-inorganic $CsPbBr_3$ perovskite nanocrystals (PNCs) was first predicted by Yu *et al.* [14]. Since then, it has been shown that the RP faults in all-inorganic PNCs can be successfully produced via multiple techniques, including: stripping passivating ligands with subsequent fusion of PNCs, doping with Mn^{2+}, and mixing halogen anions with a large atomic radius difference (e.g., Cl and I) [15-17]. Despite a number of comprehensive reports, the structure-property relationship in all-inorganic RP-PNCs remains inconclusive. This is largely due to the diversity of the inorganic materials serving as hosts of the RP faults. This includes the use of different dopants during synthesis as well as variations in the dimensionality (0D-3D) of the host materials. Along with the lack of control over formation of RP faults, elucidating the role of such RPs in optoelectronic properties remains a challenge. In this work, we estimate the exciton binding energy and lifetime in RP-$CsPbBr_3$ PNCs, and compare them to the non-RP $CsPbBr_3$ PNCs. In addition, we study the up-conversion PL response from both type of PNCs. Our findings explicitly demonstrate significant impact of RP planar faults on the properties of $CsPbBr_3$ PNCs, and therefore emphasize the urge for exploring inorganic $CsPbX_3$ PNCs with RP faults.

3.3 Methods

Transmission Electron Microscopy (TEM) images were obtained with FEI Tecnai F30 Twin 300kV Transmission Electron Microscope.

UV-vis Absorption and Photoluminescence (PL) spectra from $CsPbBr_3$ thin films, drop-casted on glass substrates, were collected with Ocean Optics USB 2000 spectrometer. UV-Vis absorption spectra from colloid samples were collected with Agilent Cary 60 UV-Vis spectrophotometer.

Upconversion Photoluminescence (UC-PL) from drop-casted thin films was obtained with a iHR320 f/4.1 spectrometer and a CCD camera from JYHoriba in a reflection geometry. The excitation wavelength of 1120-1300 nm was obtained from an optical parametric amplifier (TOPAS) using a regenerative amplifier (Spitfire Ace, Spectra Physics) with a repetition rate of 1kHz, pulse duration of 100 fs, and seeded by a Ti-Sapphire laser (Mai Tai, Spectra Physics).

Time-Resolved Photoluminescence (TR-PL) measurements were performed using a time-correlated single photon counting (TCSPC) technique. The PL lifetimes were measured with a PicoHarp 300 TCSPC module with 4 ps time resolution. The excitation wavelength of 400 nm was generated by frequency doubling the 800 nm wavelength (100 fs, 80 MHz) from a Ti-Sapphire laser (Mai Tai, Spectra Physics). The PL emission from the sample was collected by an avalanche photon counting detector module (Micro Photon Devices), using a long-pass 400 nm filter to eliminate the excitation wavelength.

3.4 Results and Discussion

3.4.1 Exciton Binding Energy

Density functional theory (DFT) calculations of the RP planar faults predicted significant band offsets in both conduction (134 meV) and valence (-193 meV) bands, as well as a higher macroscopic electrostatic potential (~1.5 eV) across the RP boundary [15, 18]. Motivated by the theoretical results in the electronic structure changes of the RP-$CsPbBr_3$ PNCs, we estimate the exciton binding energies from the experimentally obtained absorption spectra. The earlier reported bathochromic shift for colloid RP-$CsPbBr_3$ PNC was primarily attributed to a significant growth in size of the latter [15]. To tackle the size non-homogeneity, the procedure was modified to produce RP-PNCs with a smaller size deviation (*ca.* ~15 nm) from the non-RP $CsPbBr_3$ (*ca.* ~9 nm), as shown in Fig. 3.1a and b from transmission electron microscopy (TEM) images. Yet, the optical response from the colloid PNCs displayed the same characteristic features as before; there is a considerable red shift in the maximum absorption peak, but with rather negligible shift in the absorption onset and a more prominent excitonic peak at room temperature.

To estimate the binding energies, the absorption data was fitted to the Elliott's model:

$$\alpha(\omega) = \alpha_0^{3D} \frac{\hbar\omega}{E_0} \left[\sum_{n=1}^{\infty} \frac{4\pi}{n^3} \delta\left(\Delta + \frac{1}{n^2}\right) + \Theta(\Delta) \frac{\pi e^{-\pi/\sqrt{\Delta}}}{sinh\left(\pi/\sqrt{\Delta}\right)} \right], \tag{3.1}$$

where $\Delta = (\hbar\omega - E_g)/E_0$, and E_g is the band gap energy and E_0 the exciton binding energy [19].

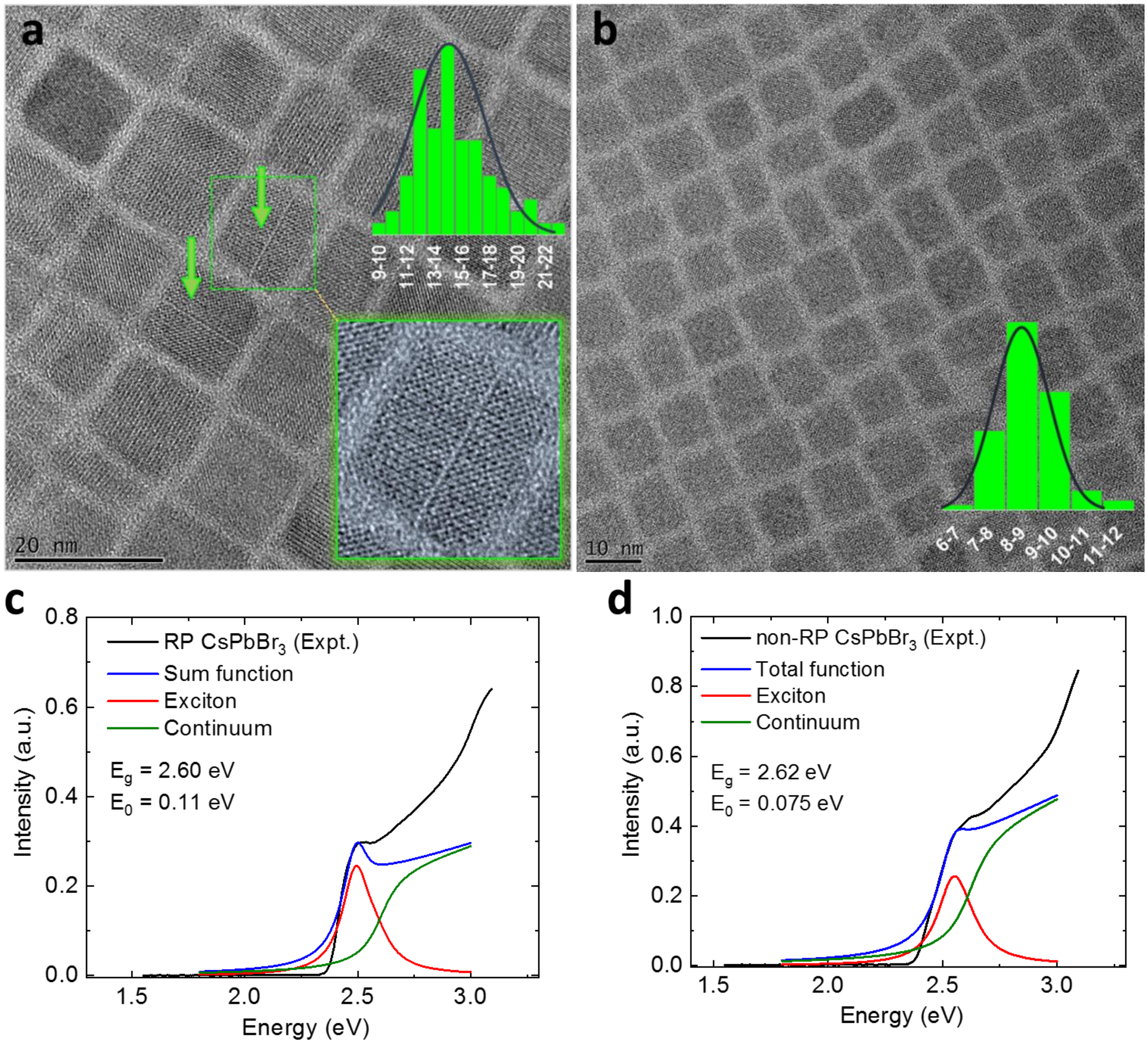

Figure 3.1. TEM images of (a) RP and (b) non-RP $CsPbBr_3$ PNCs with their size distribution. The bottom inset in panel a shows a close-up image of an RP planar fault. UV-vis absorption spectra from colloid samples (experimental and modeled) for (c) RP and (d) non-RP $CsPbBr_3$ PNCs. E_0 and E_g correspond to estimated exciton binding and band gaps energies, respectively.

The first term in the bracket represents the excitonic state and the second term describes the continuum state absorption; *n* is the principal quantum number. A Gaussian line broadening function was used for fitting the experimental absorption spectra. Interestingly, the binding energy in the colloid RP-CsPbBr$_3$ PNCs was estimated to be ~35 meV higher than that in the non-RP sample, as shown in Fig. 3.1c and d. We also analyzed the absorption spectra from drop-casted thin films of both PNCs. The binding energy in the RP-CsPbBr$_3$ film was found to be ~21 meV larger than that in the non-RP film (see Fig. 3.2).

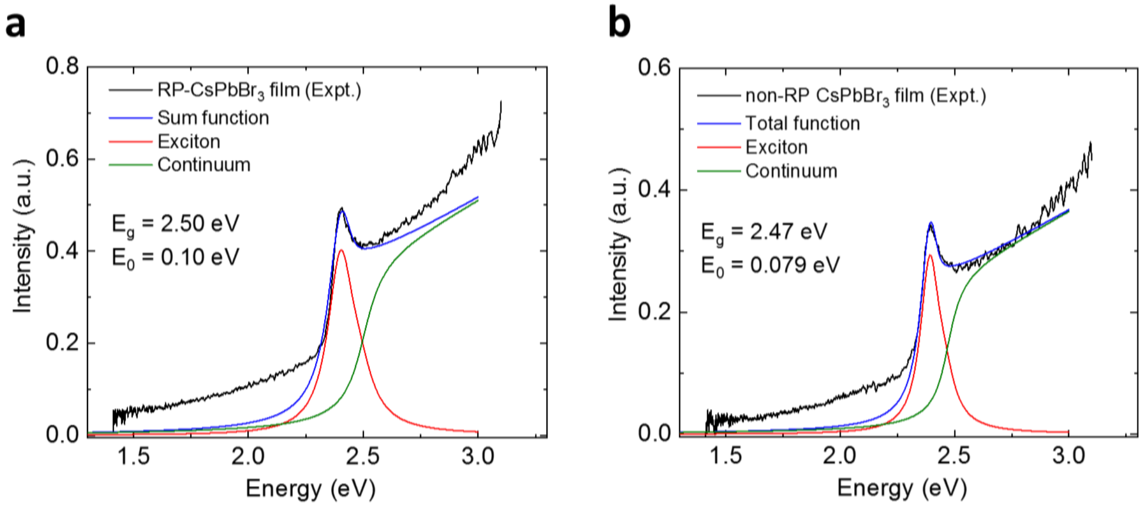

Figure 3.2. UV-vis absorption spectra for (a) RP and (b) non-RP CsPbBr$_3$ thin films (experimental and modeled).

Of note, the band gap energy derived from the RP-CsPbBr$_3$ film was found to be ~30 meV larger than the non-RP film. The observed blue shift in RP-CsPbBr$_3$ films, opposed to the red shift in the colloids, was attributed to the expansion of the band gap across the RP fault by ~327 meV, predicted with the DFT simulations, [18] and the higher probability for the occurrence of RPs in the film formation process. Due to a loss of stabilizing ligands in the RP-$CsPbBr_3$ PNCs, the latter will tend to merge due to their ionic interaction, in contrast to their high mobility in solvents.

Exciton binding energies are known to increase up to four times with a transition from 3D to 2D [20]. Even further enhancement was observed in hybrid (layered) perovskites, where the higher binding energies were attributed to an image charge effect, arising from the difference in dielectric constants between the potential well and the barrier materials [21, 22]. In our case, the RP-$CsPbBr_3$ PNCs mainly possess cuboid shape with a thickness of ~14 nm (exceeding the 2D limit) [15]. Therefore, the enhancement in the exciton binding energies is attributed to the RP fault-induced quantum confinement effect, leading to tightly bound excitons.

3.4.2 Exciton Lifetime

To investigate the effect of RP faults on the luminescent properties, we have examined the time-resolved PL decay in both types of PNCs. Figure 3.3 shows typical PL decay curves for the thin films of the RP and non-RP $CsPbBr_3$ PNCs, with PL spectra shown as insets. As seen, the presence of two relaxation modes, fast and slow, is evident for both type of PNCs. The corresponding lifetimes and amplitudes were extracted by deconvoluting the instrument response function (IRF) f_{IRF} and using that Gaussian width for the PL decay function (f_1) with lifetime τ_1 as shown below:

$$f_1(x) \times f_{IRF}(x) = \int_0^{\infty} f_1(x') f_{IRF}(x - x')\, dx', \qquad (3.2)$$

where $f_1(x) = (\mathrm{A}/\tau_1)e^{-x/\tau_1}$ and $f_{IRF}(x) = (\mathrm{A}/\sqrt{2\pi}w)e^{-(x-x_c)^2/2w^2}$. The above function can be expressed in terms of an error function:

$$f_1(x) \times f_{IRF}(x) = \frac{A}{2\,\tau_1} e^{\left[\frac{w}{2\tau_1} - \frac{x-x_C}{\tau_1}\right]}\left[1 + \mathrm{erf}(Z/\sqrt{2})\right], \qquad (3.3)$$

where $Z = (x - x_c)/w - w/\tau_1$. Since the PL decay from the samples fit with two lifetimes, we use:

$$f_1(x) \times f_{IRF}(x) + f_2(x) \times f_{IRF}(x), \qquad (3.4)$$

where $f_2(x) = (\mathrm{B}/\tau_2)e^{-x/\tau_2}$.

Remarkably, we observed a substantial difference in the exciton lifetimes. The non-RP $CsPbBr_3$ PNCs were characterized by an average exciton lifetime of ~3.5 ns, whereas the lifetime in RP-$CsPbBr_3$ was found to be more than two times larger at ~7.8 ns.

Longer exciton lifetime in RP-$CsPbBr_3$ PNCs could potentially arise from a spatial electron-hole separation across the RP fault, similar to that reported for other quantum dots with type II energy band alignment [23]. As such, if the perovskite domains, separated by RP faults, possess different band gaps originating from the difference in grain size, the excited electron would funnel into the domain with a smaller band gap, occupying the lowest available energy level, as illustrated in Figure 3.4. Given the fine thickness of the RP fault (~3.59 Å) and the observation of electron funneling in layered perovskites with considerably thicker organic spacers [24], we postulate that the proposed transition is highly probable in RP-$CsPbBr_3$ PNCs.

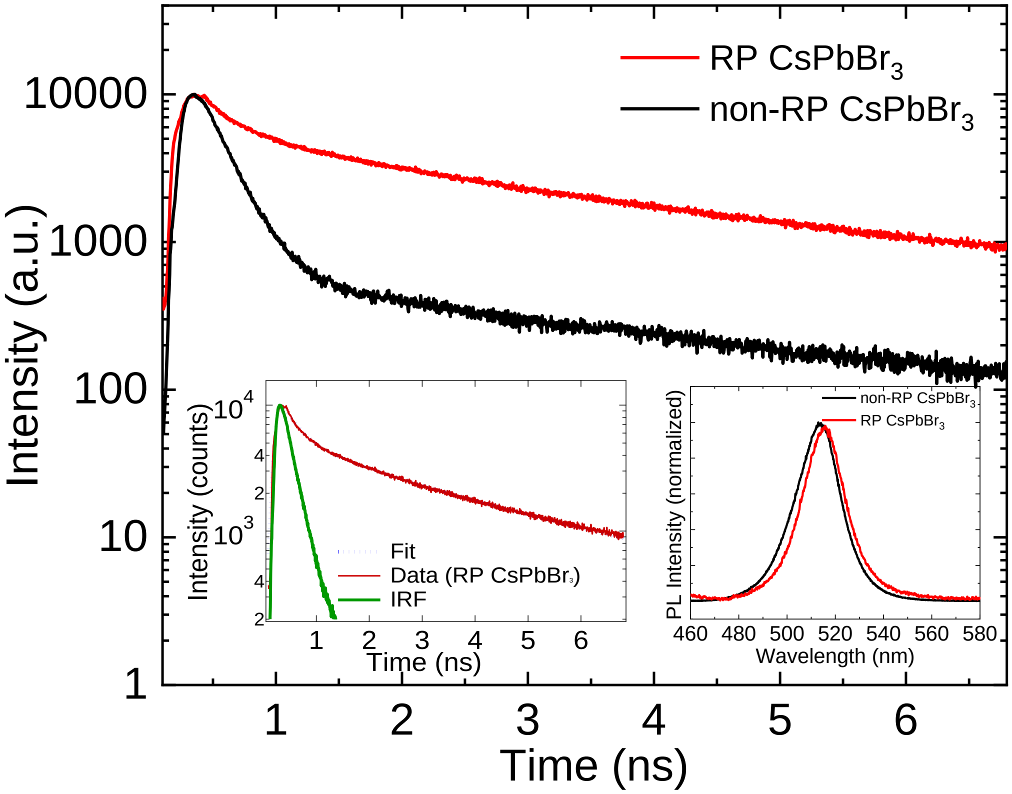

Figure 3.3. PL relaxation curves for RP and non-RP $CsPbBr_3$ PNCs. The insets show the instrument response function along with fitted decay data for RP-$CsPbBr_3$ (left) and the normalized PL spectra from the two samples (right).

The percentage contribution and lifetimes for each of the components are summarized in Table 3.1. The PL emission in the non-RP-$CsPbBr_3$ thin films was mainly driven by the exciton (band-edge) recombination (~67%). Whereas in the RP-$CsPbBr_3$ thin films the contribution from a short component dropped down to ~17%, and the PL emission was primarily determined by the long relaxation mode generally associated with trapped luminescence [25].

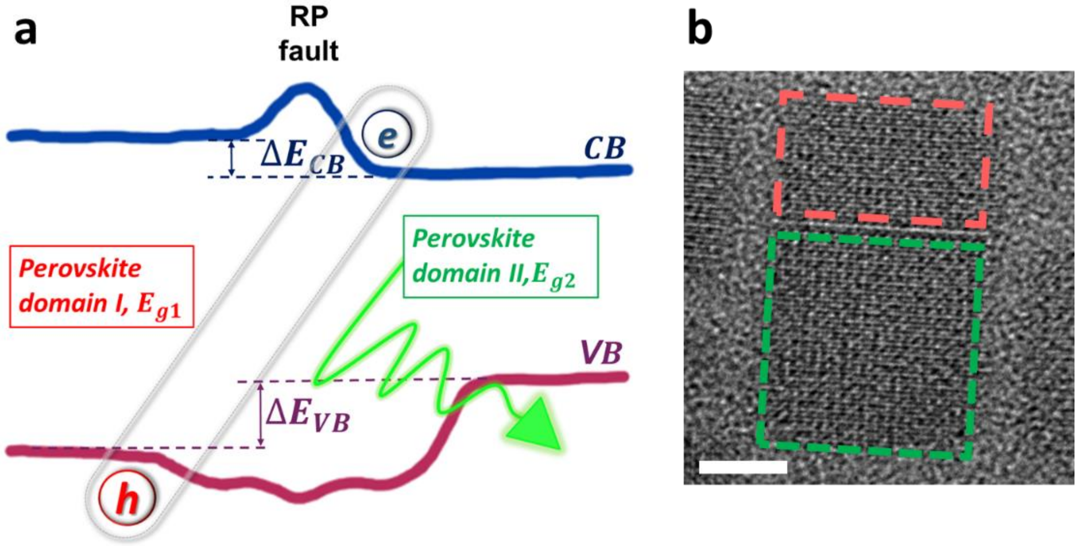

Figure 3.4. (a) Schematic illustration of spatial electron-hole separation across the RP fault. Both valence and conduction bands were drawn to replicate the shape predicted by the DFT study in [18]. (b) TEM image of the RP-$CsPbBr_3$ PNC where such phenomenon is suggested to occur. The white bar in panel b corresponds to 5 nm.

Table 3.1. Percentage contribution and exciton lifetimes corresponding to the short and long relaxation modes for RP and non-RP $CsPbBr_3$ PNCs. Short component corresponds to the recombination from the initially populated band-edge states. Long component is thought to originate from the trapped PL.

	Long component		***Short component***	
	A(%)	$\tau_1(ns)$	***B(%)***	$\tau_2(ns)$
non-RP	33	3.24±0.28	67	0.24±0.01
RP	83	3.07±0.07	17	0.30±0.02

*A,B are the fitting constants in the PL decay functions

It is evident that the formation of RP faults in $CsPbBr_3$ PNCs has a major impact on the nature of the PL emission. Trapped luminescence in semiconductor quantum dots is believed to arise from sub-gap trap states or surface states [26]. It has been widely accepted that $CsPbBr_3$ PNCs possess high defect tolerance, meaning that most point defects are shallow and do not introduce deep level states capable of trapping charge carriers [27]. Furthermore, the DFT-based calculations of all plausible point defects at the RP boundaries did not predict any sub-gap states, except Pb dangling bonds, similar to non-RP PNCs [18]. In addition, TEM image analysis of the experimentally developed RP faults did not reveal any defects in the CsBr layers [18]. However, multi-exponential PL decay combined with the existence of up-conversion PL (UC-PL), discussed in detail in the next section, in all-inorganic PNCs suggest the existence of intermediate sub-gap states [28-30]. Given the specific approach used for the formation of RP faults in our $CsPbBr_3$ PNCs, in particular stripping of stabilizing ligands from the surface of $CsPbBr_3$, we believe that the trapped luminescence is realized via surface states, which are exposed due to a reduced density of passivating ligands on the RP-$CsPbBr_3$ PNCs. The sub-gap surface states may serve as a reservoir for the excited states. However, despite that the surface states are involved in light emission, the removal of the passivating ligands does not reduce the overall PL quantum yield [15]. Consequently, the RP faults allow an efficient process for re- and de-population of the sub-gap states in the RP PNCs.

3.4.3 Up-conversion Photoluminescence

We have measured the UC-PL in both type of $CsPbBr_3$ PNCs. Thin films were drop-casted onto glass substrates, and excited with pulsed laser excitation below the energy band gap, in the range of 1120-1300 nm, as shown in Fig. 3.5 a and b.

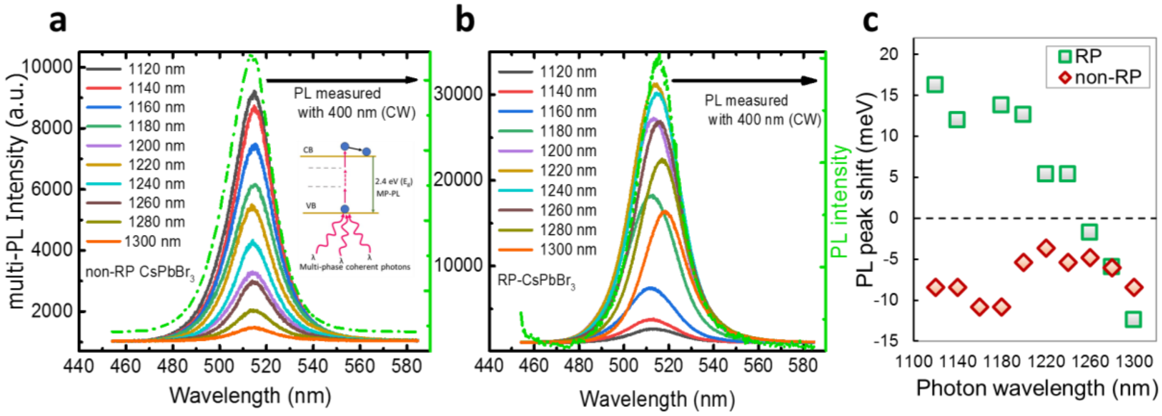

Figure 3.5. Up-conversion photoluminescence spectra taken from (a) non-RP $CsPbBr_3$ and (b) RP-$CsPbBr_3$ PNCs with their corresponding CW PL (green). The inset in panel a illustrates the mechanism for multiphoton absorption. (c) Comparative analysis of the UC-PL peak position shift with respect to CW PL. Position of the CW PL measured at 400 nm peak is assigned to 0.

The spectra were then compared to the continuous wave (CW) PL, collected with a 400 nm excitation source, to estimate the shift in the maximum PL peak position. A striking difference was discovered in the UC-PL response from both RP and non-RP $CsPbBr_3$ films, which is presented in Fig. 3.5c. The data acquired from the non-RP $CsPbBr_3$ is in good agreement with previous results of UC-PL in $CsPbBr_3$ PNCs [29, 30]. Specifically, the

UC-PL intensity increased at higher excitation energy and displayed a characteristic bathochromic shift with respect to the CW PL. Whereas, the UC-PL in RP-$CsPbBr_3$ PNCs was characterized by the bathochromic shift in the range of 1300-1260 nm, with an apparent hypsochromic shift starting at ~1240 nm. Furthermore, the UC-PL intensity in the 1300-1260 nm excitation range, measured under the same conditions, was significantly stronger in the RP-PNCs than in the non-RP PNCs. Intriguingly, around the transition point to higher emission energies, the UC-PL intensities in the RP-film start decreasing. We speculate that the red shift in UC-PL spectra in both type of PNCs stems from the recombination of the excited carriers from the surface states, located below the conduction band, to the valence band. Assuming that the RP-PNCs possess higher density of such states, due to the aforementioned loss of stabilizing ligands, the higher binding energies in RP films prevent excitons from dissociation and therefore result in stronger UC-PL. It is likely that the blue shift occurs when the excited electrons recombine from the states above the conduction minimum band [31]. However, since the hypsochromic shift in UC-PL spectra is specific to RP-films only, it would be reasonable to attribute it to the presence of RPs, precisely to the expansion of the band gap across the RP boundary by ~327 meV [18]. The obtained data explicitly shows a substantial impact of the RPs on the optoelectronic properties of the $CsPbBr_3$ PNCs.

3.5 Conclusions

In summary, our findings suggest that the formation of RP planar faults in $CsPbBr_3$ PNCs has a substantial impact on the optoelectronic properties of the latter. Specifically, we found that the RP-$CsPbBr_3$ PNCs possessed higher exciton binding energy and exhibited longer exciton lifetimes. The increase in binding energies was attributed to the RP-induced quantum confinement of excitons within the perovskite grains, cleaved by the insulating CsBr bi-layers. Longer exciton lifetimes were ascribed to the spatial electron-hole separation and were suggested to originate from the surface states. The latter appear due to the removal of the stabilizing ligands and serve as a reservoir for the excited states, while the RP faults allow their efficient repopulation.

3.6 Acknowledgements

We express deep gratitude to Prof. Suchi Guha for a paramount contribution in the studies of binding energies, time-resolved and up-conversion photoluminescence. We would also like to thank Payal Bhattacharya for performing UC-PL measurements.

3.7 References

[1] Ruddlesden, S.N.; Popper, P. New Compounds of the K_2NiF_4 Type. *Acta Crystallogr.* **1957**, 10, 538–539.

[2] Ruddlesden, S. N.; Popper, P. The Compound $Sr_3Ti_2O_7$ and Its Structure. *Acta Crystallogr.* **1958**, 11, 54-55.

[3] Dwiwedi, A.; Cormack, A. N.; Crystal Chemistry of Ruddlesden-Popper Type Structures in High T_c Ceramic Superconductors. *Bull. Mater. Sci.* **1991**, 14, 575-584.

[4] Battle, P. D.; Blundell, S. J.; Green, M. A.; Hayes, W.; Honold, M.; Klehe, A. K.; Laskey, N. S.; Millburn, J. E.; Murphy, L.; Rosseinsky, M. J.; Samarin, N. A.; Singleton, J.; Sluchanko, N. E.; Sullivan, S. P.; Vente, J. F. Colossal Magnetoresistance in $Sr_{2-x}Nd_{1+x}Mn_2O_7$ (x=0.0, 0.1). *J. Phys.: Condens. Matter* **1996**, 8, L427-L434.

[5] Birol, T.; Benedek, N. A.; Fennie, C. Interface Control of Emergent Ferroic Order in Ruddlesden-Popper $Sr_{n+1}Ti_nO_{3n+1}$. *J. Phys. Rev. Lett.* **2011**, 107,257602.

[6] Oh, Y. S.; Luo, X.; Huang, F. T.; Wang, Y.; Cheong, S. W. Experimental Demonstration of Hybrid Improper Ferroelectricity and the Presence of Abundant Charged Walls in $(Ca,Sr)_3Ti_2O_7$ Crystals. *Nat. Mater.* **2015**, 14 (4), 407−413.

[7] Chen, Z.; Guo, Y.; Wertz, E.; Shi, J. Merits and Challenges of Ruddlesden-Popper Soft Halide Perovskites on Electro-Optics and Optoelectronics. *Adv Mater.* **2018**, 31, 1, 1803514.

[8] Tsai, H.; Nie, W.; Blancon, J. C.; Stoumpos, C. C.; Asadpour, R.; Harutyunyan, B.; Nuekirch, A. J.; Verduzko, R.; Crochet, J. J.; Tretiak, S.; Pedesseau, L.; Even, J.; Alam, M. A.; Gupta, G.; Lou, J.; Ajayan, P. M.; Bedzyk, M. J.; Kanatzidis, M. G.; Mohite, A. D. High-Efficiency Two-Dimensional Ruddlesden-Popper Perovskite Solar Cells. *Nature* **2016**, 536, 312-317.

[9] Cao, D. H.; Stoumpos, C. C.; Farha, O. K.; Hupp, J. T.; Kanatzidis, M. G. 2D Homologous Perovskites as Light-Absorbing Materials for Solar Cell Applications. *J. Am. Chem. Soc.* **2015**, 137, 24, 7843–7850.

[10] Tsai, H.; Nie, W.; Blancon, J.-C.; Stoumpos, C. C.; Soe, C. M. M.; Yoo, J.; Crochet, J.; Tretiak, S.; Even, J.; Sadhanala, A.; Azzellino, G.; Brenes, R.; Ajayan, P. M.; Bulović, V.; Stranks, S. D.; Friend, R. H.; Kanatzidis, M. G.; Mohite, A. D. Stable Light-Emitting Diodes Using Phase-Pure Ruddlesden-Popper Layered Perovskites. *Adv. Mater.* **2018**, 30, 1704217.

[11] Yang, X.; Zhang, X.; Deng, J.; Chu, Z.; Jiang, Q.; Meng, J.; Wang, P.; Zhang, L.; Yin, Z.; You, J. Efficient Green Light-Emitting Diodes Based on Quasi-Two-Dimensional Composition and Phase Engineered Perovskite with Surface Passivation. *Nat Commun* **2018**, 9**,** 570.

[12] Wang, N.; Cheng, L.; Ge, R.; Zhang, S.; Miao, Y.; Zou, W.; Yi, C.; Sun, Y.; Cao, Y.; Yang, R.; Wei, Y.; Guo, Q.; Ke, Y.; Yu, M.; Jin, Y.; Liu, Y.; Ding, Q.; Di, D.; Yang, L, Xing, G.; Tian, H.; Jin, C.; Gao, F.; Friend, R. H.; Wang, J.; Huang, W. Perovskite Light-Emitting Diodes Based on Solution-Processed Self-Organized Multiple Quantum Wells. *Nature Photon* **2016**, 10**,** 699–704.

[13] Chen, Y.; Sun, Y.; Peng, J.; Tang, J.; Zheng, K.; Liang, Z. 2D Ruddlesden-Popper Perovskites for Optoelectronics. *Adv Mater.* **2017**, 30, 2, 1703487.

[14] Yu, Y.; Zhang, D.; Yang, P. Ruddlesden-Popper Phase in Two-Dimensional Inorganic Halide Perovskites: A Plausible Model and Supporting Observations. *Nano Lett*. **2017**, 17, 9, 5489–5494.

[15] Morrell, M. V.; He, X.; Luo, G.; Thind, A. S.; White, T. A.; Hachtel, J. A.; Borisevich, A. Y.; Idrobo, J. C.; Mishra, R.; Xing, Y. Significantly Enhanced Emission Stability of $CsPbBr_3$ Nanocrystals via Chemically Induced Fusion Growth for Optoelectronic Devices. *ACS Appl. Nano Mater.* **2018**, 1, 6091-6098.

[16] Paul, S.; Bladt, E.; Richter, A. F.; Döblinger, M.; Tong, Y.; Huang, H.; Dey, A.; Bals, S.; Debnath, T.; Polavarapu, L.; Feldmann, J. Manganese Doping Induced Quantum Confinement within Host Perovskite Nanocrystals through Ruddlesden-Popper Defects. *Angew. Chem. Int. Ed.* **2020**, 59, 17, 6794-6799.

[17] Akkerman, Q. A.; Bladt, E.; Petralanda, U.; Dang, Z.; Sartori, E.; Baranov, D.; Abdelhady, A. L.; Infante, I.; Bals, S.; Manna, L. Fully Inorganic Ruddlesden−Popper Double Cl−I and Triple Cl−Br−I Lead Halide Perovskite Nanocrystals. *Chem. Mater.* **2019**, 31, 2182−2190.

[18] Thind, A. S.; Luo, G.; Hachtel, J. A.; Morrell, M. V.; Cho, S. B.; Borisevich, A. Y.; Idrobo, J.-C.; Xing, Y.; Mishra, R. Atomic Structure and Electrical Activity of Grain Boundaries and Ruddlesden–Popper Faults in Cesium Lead Bromide Perovskite. *Adv. Mater.* **2019**, 31, 1805047.

[19] Haug, H., Koch, S. W. Quantum theory of the optical and electronic properties of semiconductors. World Scientific **2004**.

[20] Shinada, M.; Sugano, S. Interband Optical Transitions in Extremely Anisotropic Semiconductors. Bound and Unbound Exciton Absorption. *Phys. Soc. Japan* 21, **1966**, 1936-1946.

[21] Ishihara, T. Optical Properties of PbI-based Perovskite Structures. *J. Lumin.*, **1994**, 60-61, 269-274.

[22] Tanaka, K.; Takahashi, T.; Kondo, T.; Umebayashi, T.; Asai, K.; Ema, K. Image Charge Effect on Two-Dimensional Excitons in an Inorganic-Organic Quantum-Well Crystal. *Phys. Rev. B* 71, **2005**, 045312.

[23] Xu, F.; Volkov, V.; Zhu, Y.; Bai, H.; Rea, A.; Valappil, N. V.; Su, W.; Gao, X.; Kuskovsky, I. L.; Matsui, H. Long Electron-Hole Separation of ZnO-CdS Core-Shell Quantum Dots. *J. Phys. Chem. C* **2009,** *113*, 19419–19423.

[24] Yuan, M.; Quan, L. N.; Comin, R.; Walters, G.; Sabatini, R.; Voznyy, O.; Hoogland, S.; Zhao, Y.; Beauregard, E. M.; Kanjanaboos, P.; Lu, Z.; Kim, D. H.; Sargent, E. H. Perovskite Energy Funnels For Efficient Light-Emitting Diodes. *Nat. Nanotechnol.* 11, **2016**, 872–877.

[25] Wu, W.; Gao, Y.; Chang, Q.; Ye, H.; Zheng, Z.; Liu, W.; Li, A.; Yang, Y. Upconversion Luminescent Characteristics and Peak Shift of CdSeS Nanocrystals under Different Wavelength Laser Excitation. *J. Nanopart. Res.* **2011**, 13, 1049–1061.

[26] Peterson, M. D.; Cass, L. C.; Harris, R. D.; Edme, K.; Sung, K.; Weiss, E. A. The Role of Ligands in Determining the Exciton Relaxation Dynamics in Semiconductor Quantum Dots. *Annu. Rev. Phys. Chem.* 65, **2014**, 317-339.

[27] Kang, J.; Wang, L. W. High Defect Tolerance in Lead Halide Perovskite $CsPbBr_3$. *J. Phys. Chem. Lett.* **2017**, 8, 489−493.

[28] Koscher, B. A.; Swabeck, J. K.; Bronstein, N. D.; Alivisatos, A. P. Essentially Trap-Free $CsPbBr_3$ Colloidal Nanocrystals by Postsynthetic Thiocyanate Surface Treatment. *J. Am. Chem. Soc.* **2017**, 139, 6566-6569.

[29] Ye, S.; Zhao, M.; Yu, M.; Zhu, M.; Yan, W.; Song, J.; Qu, J. Mechanistic Investigation of Upconversion Photoluminescence in All-Inorganic Perovskite $CsPbBrI_2$ Nanocrystals. *J. Phys. Chem. C* **2018**, 122, 3152−3156.

[30] Wang, Y.; Li, X.; Zhao, X.; Xiao, L.; Zeng, H.; Sun, H. Nonlinear Absorption and Low-Threshold Pumped Stimulated Emission from All-Inorganic Perovskite Nanocrystals. *Nano Lett.* **2016**, 16, 448-453.

[31] Mandal, S.; Mukherjee, S.; De, C. K.; Roy, D.; Ghosh, S.; Mandal, P. K. Extent of Shallow/Deep Trap States beyond the Conduction Band Minimum in Defect-Tolerant $CsPbBr_3$ Perovskite Quantum Dot: Control over the Degree of Charge Carrier Recombination. *J. Phys. Chem. Lett.* **2020**, 11, 1702−1707.

CHAPTER IV. $CsPbBr_3$-BASED THIN FILM LIGHT EMITTING DEVICES WITH AND WITHOUT RUDDLESDEN-POPPER PLANAR FAULTS

4.1 Abstract

Earlier we demonstrated that the RP-$CsPbBr_3$ PNCs possess larger binding energies, longer exciton lifetimes, and an exceptionally higher resistance to photodegradation compared to the non-RP $CsPbBr_3$ PNCs. The properties stated above are highly desired for efficient and bright LEDs. Driven by our findings, we put RP-$CsPbBr_3$ PNCs to a test in a number of light emitting structures. To our knowledge, this is the first demonstration of the all-inorganic RP-$CsPbBr_3$-based LED. We postulate and experimentally verify that the LEDs based on $CsPbBr_3$ PNCs with the RPs significantly outperform LEDs without RPs. The comparison was made based on the devices with and without electron transporting layers.

4.2 Introduction

While the research in all-inorganic RP-type perovskites is just beginning to evolve, hybrid RP-perovskites have already established themselves as promising candidates for a variety of optoelectronic applications [1-9]. Organic-inorganic perovskite-based photovoltaics has been recognized as the fastest developing solar cell technology, and is predicted to surpass its main competitor – silicon. As such, the efficiency of hybrid perovskite solar cells jumped from 3.8% to 22.1% in within less than a decade [10]. However, the progress is significantly hindered by the inherent susceptibility of hybrid perovskites to moisture, light, and high temperatures [11, 12].

The air stability of hybrid perovskites is shown to be significantly improved by introducing an RP phase into perovskite domains [13, 14]. As such, 2D hybrid perovskite slabs, which serve as potential wells, are sandwiched between organic spacers, which serve as potential barriers. The hydrophobic nature of the organic spacers result in a considerable enhancement of overall air stability. However, such improvement was achieved at the cost of other favorable properties. Owning to its insulating nature, organic spacers can significantly impede electron transport, resulting in lower carrier mobility, charge accumulation and recombination losses [2]. Efforts have been made by reducing the length of organic spacers.

The challenges stated above can be resolved by utilizing all-inorganic RP-$CsPbBr_3$ PNCs with naturally occurring ultrathin RP planar faults. Owning to the fine thickness, CsBr layers are predicted to allow charge funneling between enclosed domains without constraining charge transport (described in Chapter 3.4.2). In addition, RP-$CsPbBr_3$ were shown to possess larger binding energies and longer exciton lifetimes. High binding energies prevent exciton dissociation, and therefore facilitate radiative recombination. Combined with an exceptional emission stability, the RP-$CsPbBr_3$ PNCs present themselves as excellent candidates for LEDs. In this study, for the first time such all-inorganic RP- PNCs are evaluated in thin film light emitting structures, and are shown to outperform LEDs with non-RP PNCs.

4.3 Methods

4.3.1 Device Fabrication

Pre-patterned ITO substrates (Ossila, 20 Ω/square) were cleaned using ultrasonication in acetone and isopropanol for 10 mins respectively, rinsed with deionized water, and dried with nitrogen. ITO substrates were then treated with oxygen plasma for 10 mins. PEDOT:PSS (Poly(3,4-ethylenedioxythiophene) polystyrene sulfonate) solution (CLEVIOS™ P VP AI 4083) was deposited using spin-coater at 5000 rpm for 60 sec, and annealed at 140°C for 15 mins under nitrogen environment. Subsequently, perovskite layer was deposited at 2000 rpm for 60 sec and annealed in the air at 70°C for 30 mins. $PC_{60}BM$ ([6,6]-Phenyl-C61-butyric acid methyl ester) was dissolved in chloroform and 1,4-diclorobenzene in [1:1] ratio and deposited on top of perovskite at 900 rpm for 60 sec, following annealing in the air for 5 mins at 115°C. Ca and Al or Au were deposited sequentially using thermal evaporation. All devices were encapsulated using light-curable epoxy (Ossila).

4.3.2 Device Characterization

Current density-voltage (*J-V*) characteristics were measured using Keithley 2400 source-meter unit.

The electroluminescence spectra for the devices were collected using Ocean Optics USB 2000 spectrometer.

The emissive area of the devices was estimated from the images using ImageJ software. The study on the morphology and the energy-dispersive X-ray spectroscopy (EDS) analysis of the perovskite films deposited on ITO/PEDOT:PSS glass substrates were performed with FEI Quanta 600 FEG Environmental Scanning Electron Microscope (SEM).

4.4 Results and Discussion

4.4.1 ITO/PEDOT:PSS/Perovskite/PC$_{60}$BM/Ca/Al LEDs

Both type of PNCs were tested in the LEDs with ITO/PEDOT:PSS/Perovskite/PC$_{60}$BM/Ca/Al architecture. For simplicity, the LEDs assembled using PNCs with and without RP faults are referred as 'RP' and 'control', respectively. PC$_{60}$BM is a common choice for n-type layer in thin film LEDs and primarily works as an electron-transporting layer (ETL).

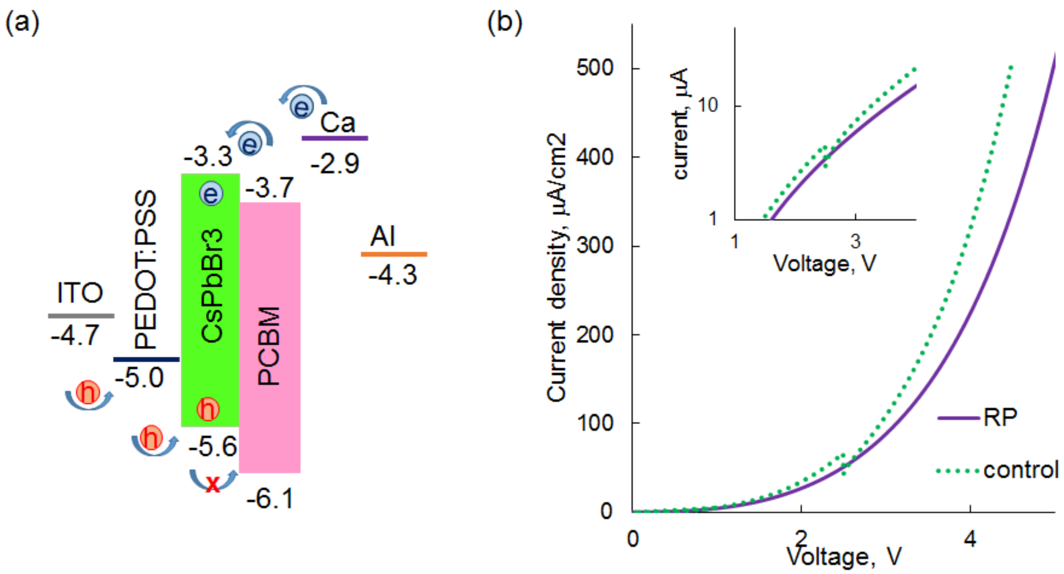

Figure 4.1. (a) Energy diagram of the ITO/PEDOT:PSS/Perovskite/PC$_{60}$BM/Ca/Al LED. (b) Current density-voltage characteristics for the LEDs with (purple) and without (green) RPs. Inset shows current at logarithmic scale.

It is worth pointing out that in the proposed architecture PC$_{60}$BM serves as a hole-blocking layer (HBL) rather than ETL as shown in Figure 4.1a. Al was deposited on top of Ca to prevent cathode oxidation. Comparative analysis of RP and control LEDs show that both devices display relatively similar current-density characteristics and turn-on voltage (Fig.

4.1b). As expected both devices demonstrate stronger electroluminescence (EL) with higher voltage applied. However, RP LEDs exhibit a significantly stronger EL response under same conditions (Figure 4.2).

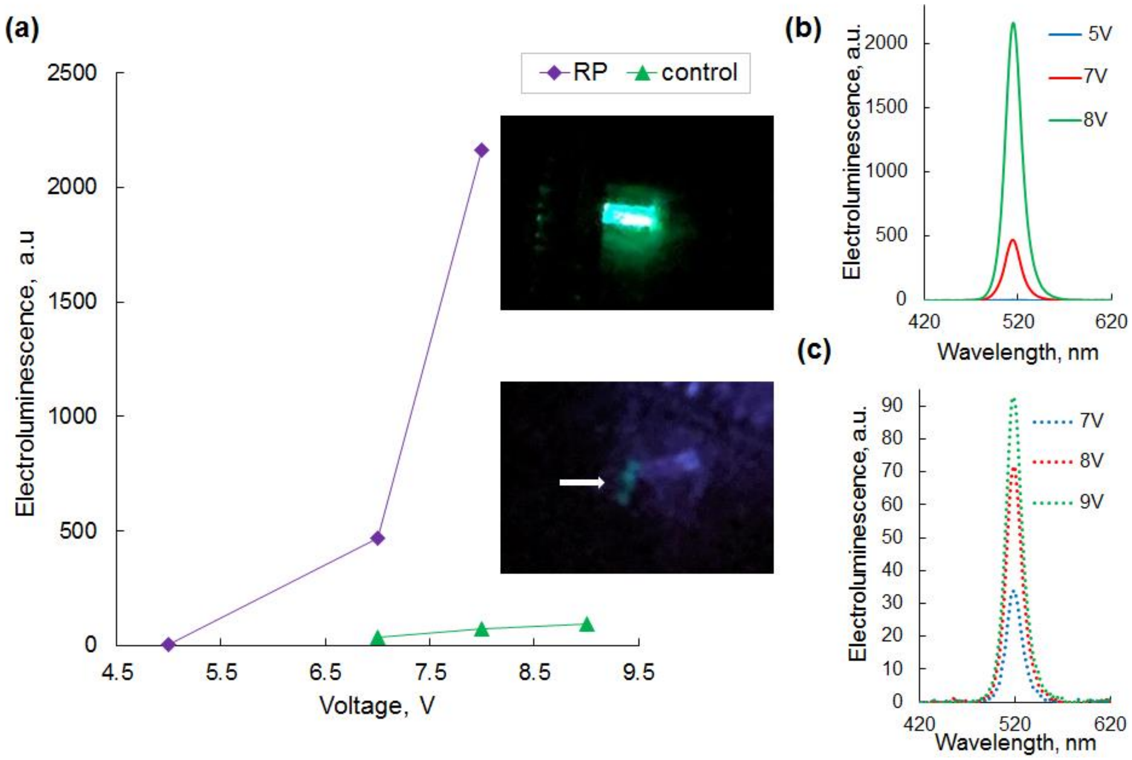

Figure 4.2. (a) Comparative analysis of the electroluminescence response from the RP (purple) and control (green) LEDs. The insets show the photos of the RP (top) and control (bottom) devices taken in the dark under same voltage applied. EL spectra in (b) and (c) correspond to the data points in panel a for RP and control LED, respectively.

Considerably lower performance in the control devices could be linked to a relatively poor morphology of the perovskite film. Given the small size of $CsPbBr_3$ PNCs (*ca*. 8 nm), it is rather challenging to produce a pinhole free thin film. Pinholes in the emissive layer can lead to significant current losses and, therefore, result in low efficiency of the device. Owing to larger lateral dimensions, thin films out of RP-$CsPbBr_3$ PNCs will presumably have less grain boundaries which often carry deep level trap cites capable of capturing excitons and resulting in unfavorable nonradioactive recombination. However, our later study of the film morphology for both devices eliminates this reasoning. Findings are provided in Chapter 4.4.4. In addition, we found that the performance of the LED could be critically altered by the deposition of $PC_{60}BM$ on top of the perovskite layer, leading to poorly emissive areas as shown in Figure 4.3.

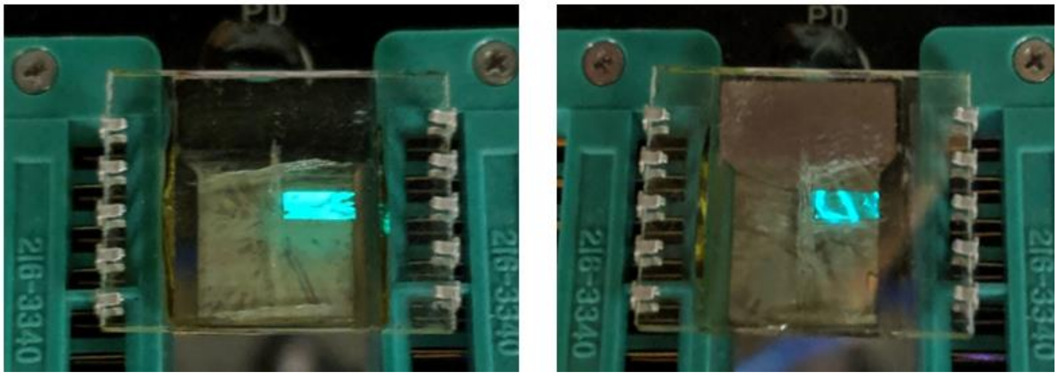

Figure 4.3. Images of RP-$CsPbBr_3$ LEDs with defect-free (left) and defective (right) emissive layers. The defects appear upon the deposition on PC60BM layer on top of the perovskite via spin-coating.

To study the impact of $PC_{60}BM$ on a perovskite layer, we collected PL response from a $PC_{60}BM/CsPbBr_3$ film for 3 independent spots with different thickness of $PC_{60}BM$ layer as depicted in Figure 4.4. We found out that a thin $PC_{60}BM$ layer on top of perovskite lead to negligible changes in PL, whereas thicker layer resulted in almost complete loss of PL.

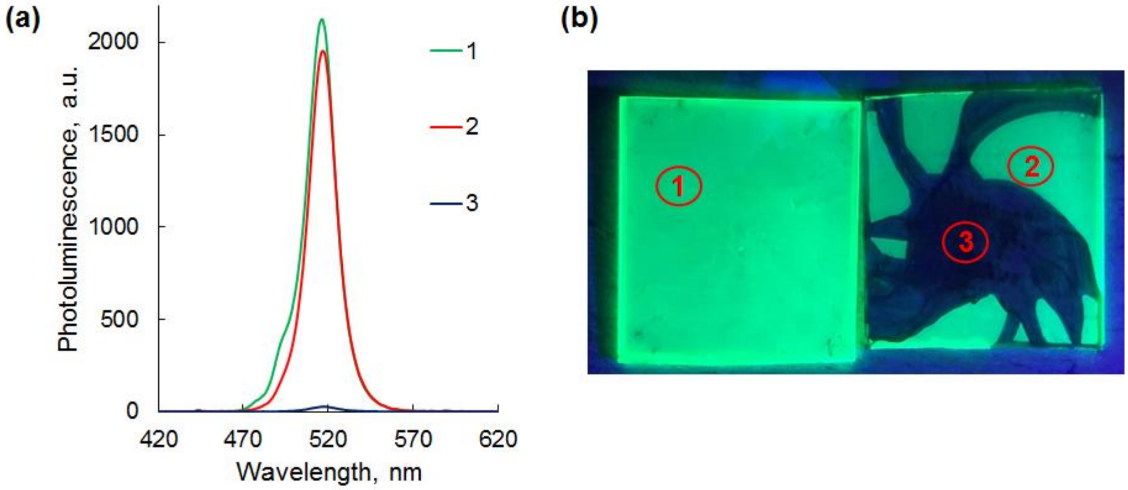

Figure 4.4. (a) PL spectra from a $PC_{60}BM/CsPbBr_3$ film corresponding to 3 independent spots with a different $PC_{60}BM$ thickness: 1 – no $PC_{60}BM$, 2 – thin $PC_{60}BM$, 3 – thick $PC_{60}BM$. (b) Images of the areas corresponding to states 1-3 in panel a.

To exclude the possibility of $PC_{60}BM$ completely etching away perovskite layer, non-emissive region 3 was tested under laser beam allowing higher resolution (Fig. 4.5). A clearly observed emission from the sample verifies that PNCs layer is not etched away. We postulate that the PL is significantly reduced due to the thickness of $PC_{60}BM$ reaching exciton diffusion limit.

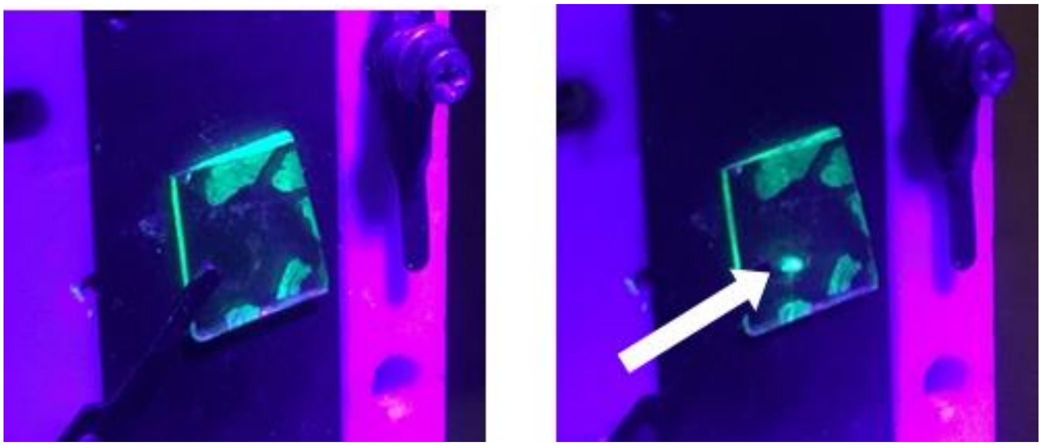

Figure 4.5. Images of non-emissive $PC_{60}BM/CsPbBr_3$ layer under UV-light without (left) and with (right) laser on. Emission from $CsPbBr_3$ induced by laser is marked by white arrow.

In conclusion, spin-coating of $PC_{60}BM$ layer on top of perovskite introduces a variable that can mislead our findings on the role of RPs. Therefore, it is imperative that the perovskite layer undergoes minimal to no alteration in the assembling process.

4.4.2 ETL-FREE ITO/PEDOT:PSS/Perovskite/Ca/Al LEDs

To eliminate the uncertainties possibly introduced by the deposition of $PC_{60}BM$ on top of perovskite we tested both types of PNCs in ETL-free devices (Fig. 4.6a). In a device with ITO/PEDOT:PSS/Perovskite/Ca/Al architecture, we find that RP LEDs generate higher currents along with a lower turn on voltage (Fig. 4.6b).

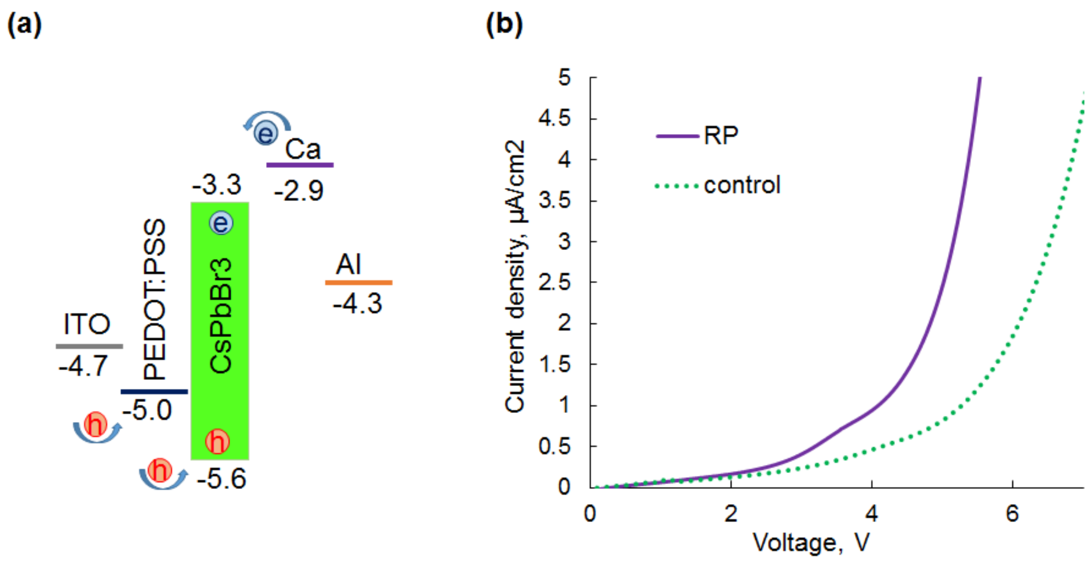

Figure 4.6. (a) Energy diagram corresponding to the architecture of the PC60BM-free LEDs. (b) Current density-voltage characteristics for RP (purple) and non-RP (green) LEDs.

When EL intensity is compared for both devices, we again observe a significantly stronger response in RP LEDs (Fig. 4.7). We postulate that the improvement is most likely attributed to the changes in optoelectronic properties of $CsPbBr_3$ PNCs induced by the presence of RP planar faults. However, the difference in EL response could also originate from the difference in the current density.

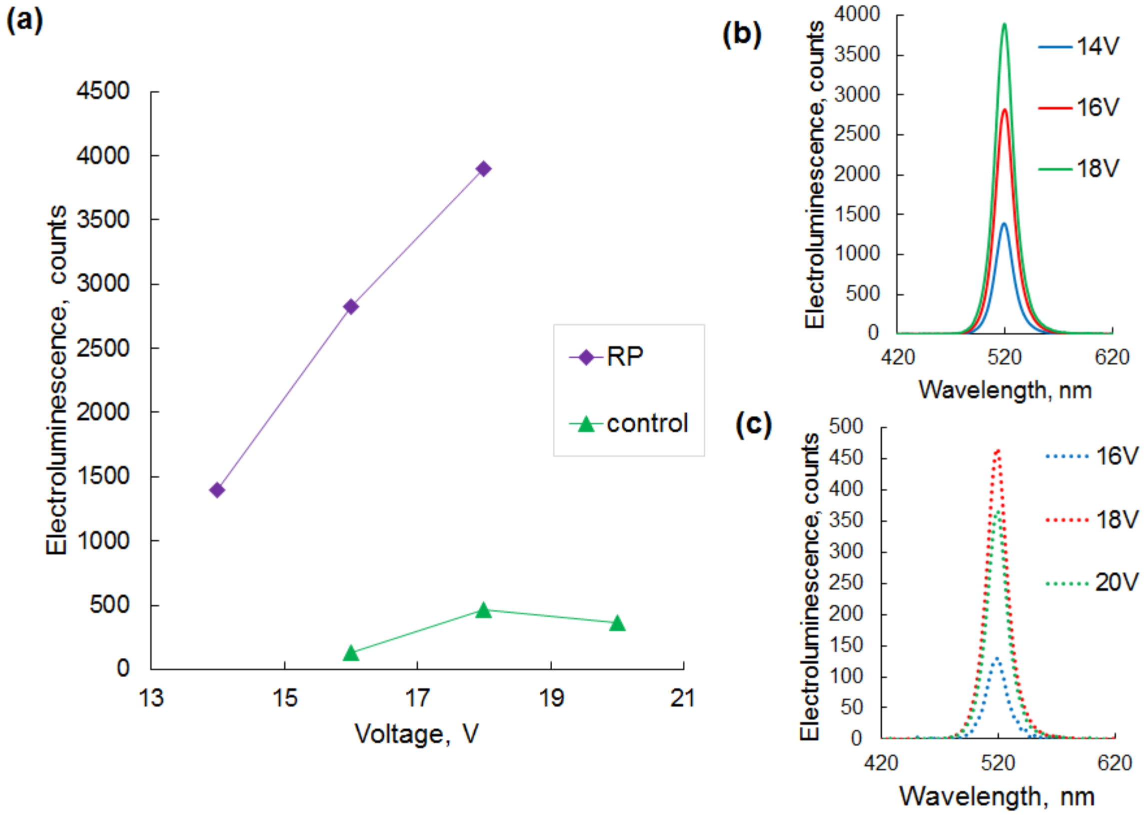

Figure 4.7. (a) Comparative analysis of the EL response from the RP (purple) and non-RP (green) LEDs. EL spectra in (b) and (c) correspond to the raw data for RP and non-RP LEDs, respectively.

An absolute measurement of the LED performance, such as an external quantum efficiency, would be the appropriate measurement to validate better performance of RP LEDs. Given technical issues, we could not perform such measurement.

4.4.3 ETL-FREE ITO/PEDOT:PSS/Perovskite/Au LEDs

As an alternative, both type of PNCs were also tested in the LEDs with ITO/PEDOT:PSS/Perovskite/Au architecture.

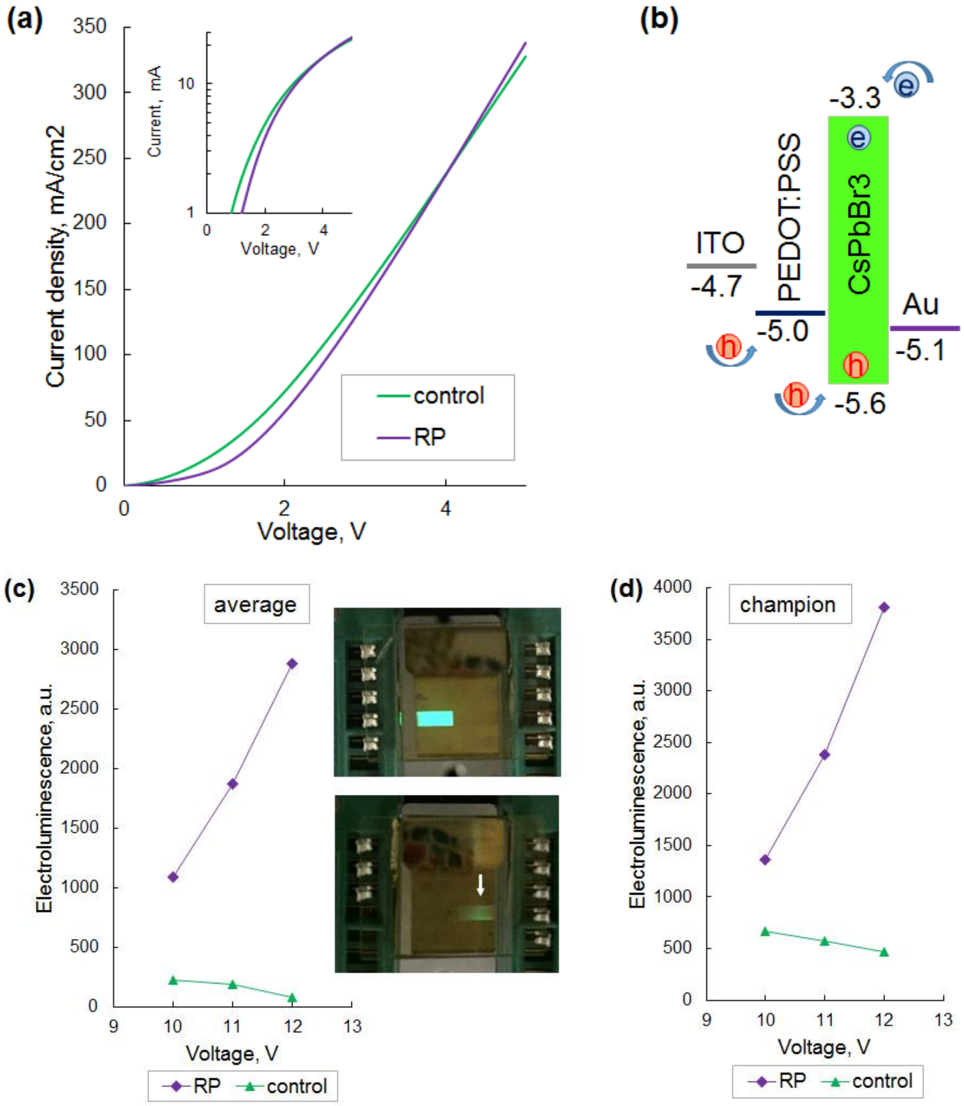

Figure 4.8. (a) Current density-voltage characteristics for LEDs with and without RPs. Inset shows current at logarithmic scale (top). (b) Energy band diagram corresponding to the ITO/PEDOT:PSS/Perovskite/Au device architecture. Comparative analysis of RP and control LED performance (c) averaged for all devices and (d) for champion LEDs. Insets in panel (c) are photos of the RP (top) and control (bottom) LEDs.

Despite reasonably close generated current density and turn-on voltage in the devices, we observe a significant improvement in EL response for RP LED (Fig. 4.8a). As seen in Figure 4.8c, the RP devices are significantly brighter. On average, the EL response from the RP device is at least 5 times stronger (at 10V) and reaches the difference as high as 36 times (at 12V). Additionally, RP LED display superior air stability. As such, higher voltage results in stronger EL intensity, whereas control LEDs suffer greatly from combination of Joule heat, electrode migration, and exposure to air. Furthermore, RP devices demonstrate higher reproducibility. The average intensity from the majority of the devices is very similar to the champion LED, whereas a drastic difference is observed with the control devices (Fig. 4.8c and d). The observed trend lead us to conclude that the RP LEDs indeed possess stronger EL intensity and higher air stability.

4.4.4 ITO/PEDOT:PSS/Perovskite Thin Film Morphology

As we mentioned earlier, the quality of the emissive layer can greatly affect the overall device performance. Thus, we studied the morphology of the perovskite films in each of the devices under Scanning Transmission Microscopy (SEM) (Fig. 4.9). Thin films of RP and non-RP $CsPbBr_3$ PNCs were produced following the steps for the LEDs fabrication to replicate the emissive layers in the devices.

The films did not exhibit significant difference in terms of compactness/porosity. Yet the RP film had a very distinct feature. We observed frequent areas of lager aggregates as depicted in Figure 4.10.

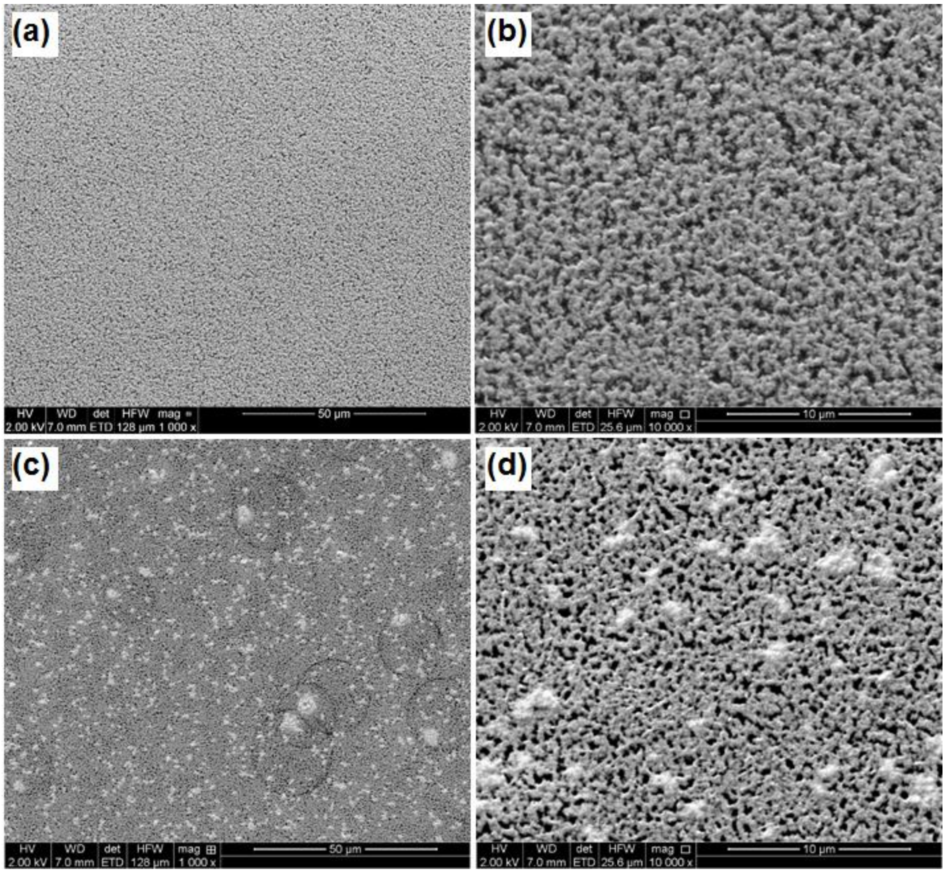

Figure 4.9. SEM images of the perovskite films (a, b) with and (c, d) without RPs. Perovskite layers are deposited on top of the ITO/PEDOT:PSS substrate to replicate layers in LEDs.

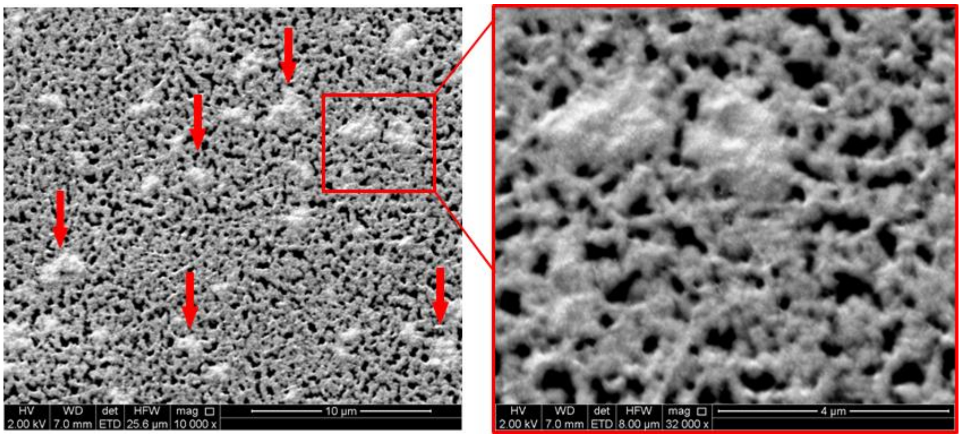

Figure 4.10. SEM image of the perovskite film with RP faults showing multiple areas with larger aggregates (marked with red arrows). Image on the right is a close up of a highlighted area.

To find out their nature we performed Energy-Dispersive X-ray (EDX) Spectroscopy analysis for the areas with and without larger aggregates. The areas of the interest are highlighted in Figure S4.1 (Section 4.7). We found that areas with larger aggregates showed a stronger response for all three atoms, including Cs, Pb, and Br (Figure S4.2), which allowed us to conclude that those areas were larger nanocrystals of $CsPbBr_3$. With the help of ImageJ software, we estimated the film porosity quantitatively from the SEM images (Fig. 4.11). Interestingly, we found that porosity of the control film on average is 3% less when compared to the RP film. Thus, we may conclude that the improved EL response in RP LEDs is attributed to the nature of the RP-PNCs.

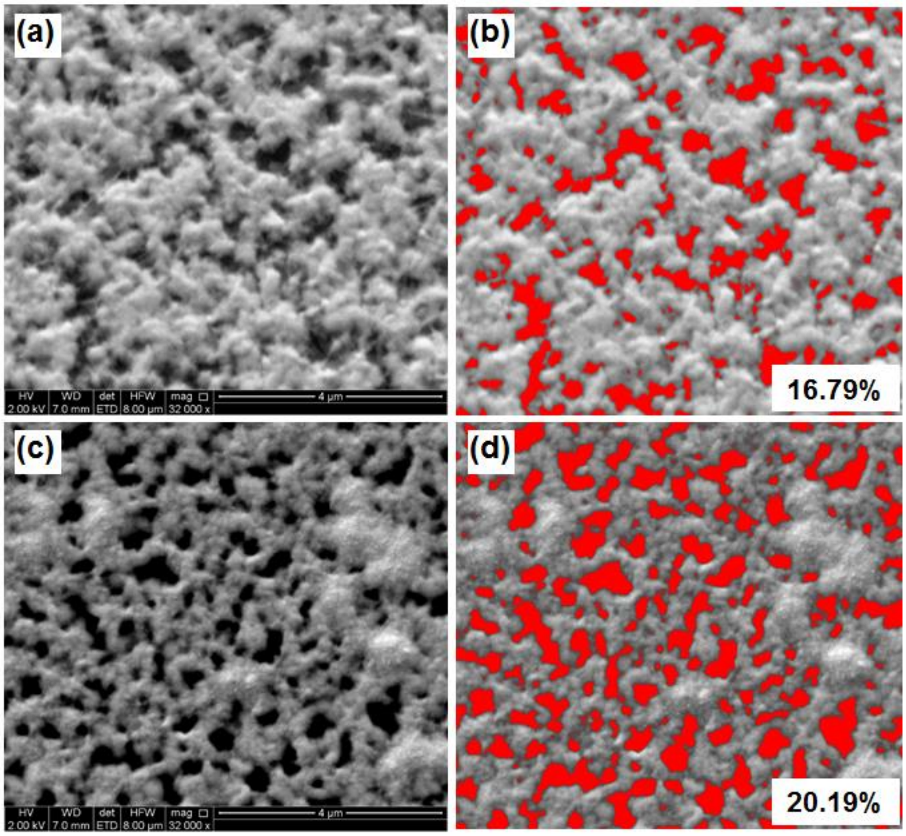

Figure 4.11. SEM images of (a) non-RP and (c) RP perovskite films with (b, d) corresponding porosity analysis, respectively.

4.5 Conclusions

In summary, RP-$CsPbBr_3$ PNCs were evaluated in thin-film perovskite LEDs, and compared to the performance of the devices without RP faults. We found that RP devices displayed substantially stronger EL response in both LEDs with and without ETL, significantly stronger air stability, and better reproducibility. The morphology of the perovskite films in both devices was studied. The porosity of the control film was estimated to be 3% lower than that of the RP film. We postulate that the observed enhancement is attributed to the presence of RP planar faults in the perovskite domains, and their impact on optoelectronic properties of the PNCs. This includes larger binding energies, longer exciton lifetimes, and improved emission stability.

4.6 Acknowledgements

We express deep gratitude to Professor Suchi Guha for providing platform for all experimental work with LEDs, and indispensable discussions of the results. We would like to acknowledge Alec Pickett for his paramount contribution in the early stages of assembling and testing LEDs. We thank David Stalla for his contribution in SEM and EDX analysis of the perovskite films.

4.7 Supplemental Information

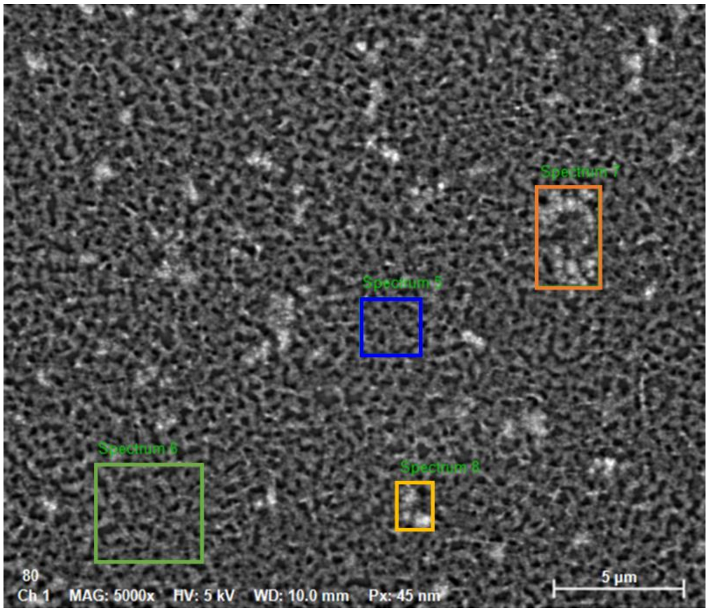

Figure S4.1. SEM image of the perovskite film with RP faults. Areas highlighted with orange and yellow correspond to areas with larger aggregates. Areas without are highlighted with green and blue.

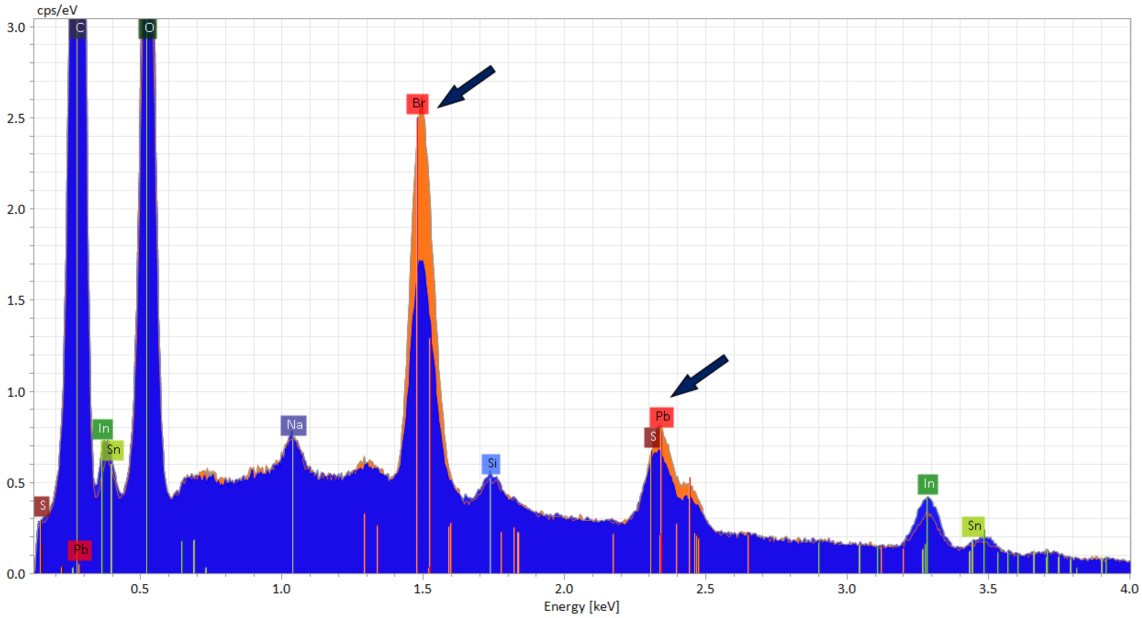

Figure S4.2. EDX spectra collected from the RP-film from the areas with (orange) and without (orange) larger $CsPbBr_3$ aggregates. Peaks corresponding to Br and Pb are marked with black arrows.

4.8 References

[1] Pedesseau, L.; Sapori, D.; Traore, B.; Robles, R.; Fang, H.H.; Loi, M. A.; Tsai, H.; Nie, W.; Blancon, J.C.; Neukirch, A.; Tretiak, S.; Mohite, A. D.; Katan, C.; Even, J.; Kepenekian, M. Advances and Promises of Layered Halide Hybrid Perovskite Semiconductors. *ACS Nano* **2016**, 10, 11, 9776–9786.

[2] Chen, Y., Sun, Y., Peng, J., Tang, J., Zheng, K., Liang, Z. 2D Ruddlesden–Popper Perovskites for Optoelectronics. *Adv. Mater.* **2018**, 30, 1703487.

[3] Chen, Z., Guo, Y., Wertz, E., Shi, J. Merits and Challenges of Ruddlesden–Popper Soft Halide Perovskites in Electro-Optics and Optoelectronics. *Adv. Mater.* **2019**, 31, 1803514.

[4] Tsai, H.; Nie, W.; Blancon, J. C.; Stoumpos, C. C.; Asadpour, R.; Harutyunyan, B.; Nuekirch, A. J.; Verduzko, R.; Crochet, J. J.; Tretiak, S.; Pedesseau, L.; Even, J.; Alam, M. A.; Gupta, G.; Lou, J.; Ajayan, P. M.; Bedzyk, M. J.; Kanatzidis, M. G.; Mohite, A. D. High-efficiency two-dimensional Ruddlesden-Popper perovskite solar cells. *Nature* **2016**, 536, 312-317.

[5] Cao, D. H.; Stoumpos, C. C.; Farha, O. K.; Hupp, J. T.; Kanatzidis, M. G. 2D Homologous perovskites as light-absorbing materials for solar cell applications. *J. Am. Chem. Soc.* **2015**, 137, 24, 7843–7850.

[6] Tsai, H.; Nie, W.; Blancon, J.-C.; Stoumpos, C. C.; Soe, C. M. M.; Yoo, J.; Crochet, J.; Tretiak, S.; Even, J.; Sadhanala, A.; Azzellino, G.; Brenes, R.; Ajayan, P. M.; Bulović, V.; Stranks, S. D.; Friend, R. H.; Kanatzidis, M. G.; Mohite, A. D. Stable light-emitting diodes using phase-pure Ruddlesden-Popper layered perovskites. *Adv. Mater.* **2018**, 30, 1704217.

[7] Yang, X.; Zhang, X.; Deng, J.; Chu, Z.; Jiang, Q.; Meng, J.; Wang, P.; Zhang, L.; Yin, Z.; You, J. Efficient green light-emitting diodes based on quasi-two-dimensional composition and phase engineered perovskite with surface passivation. *Nat Commun* **2018**, 9**,** 570.

[8] Wang, N.; Cheng, L.; Ge, R.; Zhang, S.; Miao, Y.; Zou, W.; Yi, C.; Sun, Y.; Cao, Y.; Yang, R.; Wei, Y.; Guo, Q.; Ke, Y.; Yu, M.; Jin, Y.; Liu, Y.; Ding, Q.; Di, D.; Yang, L, Xing, G.; Tian, H.; Jin, C.; Gao, F.; Friend, R. H.; Wang, J.; Huang, W. Perovskite light-emitting diodes based on solution-processed self-organized multiple quantum wells. *Nature Photon* **2016**, 10**,** 699–704.

[9] Yuan, M.; Quan, L.; Comin, R.; Walters, R.; Voznyy, O.; Hoogland, S.; Zhao, Y.; Beauregard, E. M.; Kanjanaboos, P.; Lu, Z.; Kim, D. H.; Sargent, E. H. Perovskite energy funnels for efficient light-emitting diodes. *Nature Nanotech* **2016**, 11**,** 872–877.

[10] Yang, W. S.; Park, B.; Jung, E. H.; Jeon, N. J.; Kim, Y. C.; Lee, D. U.; Shin, S. S.; Seo, J.; Kim, E. K.; Noh, J. H.; Seok, S. Iodide management in formamidinium-lead-halide−based perovskite layers for efficient solar cells. *Science* **2017**, 356, 1376−1379.

[11] Rong, Y.; Liu, L.; Mei, A.; Li, X.; Han, H. Beyond efficiency: the challenge of stability in mesoscopic perovskite solar cells. *Adv. Energy Mater.* **2015**, *5*, 1501066.

[12] Wang, Z.; Shi, Z.; Li, T.; Chen, Y.; Huang, W. Stability of perovskite solar cells: a prospective on the substitution of the A cation and X anion. *Angew. Chem. Int. Ed.* **2017**, *56*, 1190.

[13] Hong, X.; Ishihara, T.; Nurmikko, A. V. Dielectric confinement effect on excitons in PbI_4-based layered semiconductors. *Phys. Rev. B* **1992**, *45*, 6961.

[14] Smith, I. C.; Hoke, E. T.; Solis-Ibarra, D.; McGehee, M. D.; Karunadasa, H. I. A layered hybrid perovskite solar-cell absorber with enhanced moisture stability. *Angew. Chem. Int. Ed.* **2014**, 53, 11232-11235.

CHAPTER V. CONCLUSIONS AND FUTURE WORK

In summary, we demonstrated that the RP planar faults in $CsPbBr_3$ PNCs were successfully formed via post-synthetic fusion growth of the PNCs, triggered by the injection of diethylzinc. We showed that the concentration of the developed RP faults was improved when the post-synthetic growth of PNCs was performed in the excess of CsBr. We revealed an extraordinary resilience to photodegration of RP-$CsPbBr_3$ PNCs in the absence of high moisture content. We also showed that the RP faults were preserved during the anion exchange reaction with PbI_2, resulting in the formation of mixed RP-$(CsPBr/I)_3$ PNCs. In addition, we demonstrated that the formation of RPs in $CsPbBr_3$ PNCs significantly altered their optoelectronic properties. As such, RP-$CsPbBr_3$ PNCs were found to possess higher binging energies and longer exciton lifetimes. The former was attributed to the quantum confinement of excitons within the perovskite domains, cleaved by the RP faults. The latter was ascribed to a plausible spatial electron-hole separation across the RP fault similar to the one reported for other quantum dots with type II alignment. Motivated by these finding, we evaluated the potential of RP-$CsPbBr_3$ PNCs in thin film LEDs and compared it to the non-RP PNCs. We found that the RP-LEDs significantly outperformed non-RP devices in terms of EL intensity, air lifetime and reproducibility. The comparison was made based on several architectures, including with and without ETL. The work allowed us to conclude that the engineering of RP faults in $CsPbBr_3$ PNCs is an excellent pathway for the improvement of perovskite-based light emitting technology.

In light of made discoveries, we believe that further exploration of the RP-$CsPbBr_3$ PNCs is of the utmost importance. Given that such PNCs in our study were analyzed as an ensemble, whether colloid or a thin film; the next study on their optoelectronic properties should be based on a single-particle spectroscopy. This would allow to eliminate the impact of the non-RP PNCs in the ensemble (e.g. intersystem energy transfers), and therefore study the response solely from the PNCs with the RP planar faults.

In the course of our work, we also produced mixed RP-$CsPb(Br/I)_3$ PNCs which have not been reported before. Generally, the RP faults in mixed PNCs are produced when the halide ions in the perovskite structure possess substantially different radii. This includes I and Cl, or a combination of the three halides: I, Br and Cl. We successfully developed RPs in mixed $CsPb(Br/I)_3$ PNCs by the anion-exchange of RP-$CsPbBr_3$ with PbI_2. Therefore, the work opens up a new avenue for exploration of RP-$CsPb(Br/I)_3$.

VITA

Mariia Goriacheva was born in Penza, Russia, on October 24, 1990. She received the degree of Bachelor in Science in Nanotechnology from Penza State University in 2014. She entered the University of Missouri – Columbia in 2016 and received the Master of Science Degree in Chemical Engineering in 2017, followed by a Doctor of Philosophy Degree in Chemical Engineering in 2021.